Elasticity of Compressed Emulsions

Elasticity of Compressed Emulsions

A dissertation presented
by

Rodrigo Emigdio Guerra

to
Department of Physics

in partial fulfillment of the requirements
for the degree of
Doctor of Philosophy
in the subject of
Physics

Harvard University
Cambridge, Massachusetts

May 2014

Dissertation Advisor: David A. Weitz Rodrigo Emigdio Guerra

Elasticity of Compressed Emulsions

Abstract

The interfaces of bubbles and droplets imbue foams and emulsions with extraordinary mechanical and chemical properties. The remarkably large interfacial area of these structures controls their thermodynamics and makes them practical and functional materials. When these interfaces are forced to touch, they can turn a dispersion of one fluid in another into a solid. These solid-like properties are evident in common household products such as shaving foam and mayonnaise, and our ability to control the fluid and solid properties of these materials is essential to their function.

Here we present results from three studies on the mechanical properties and applications of foams and emulsions. We describe experiments designed to probe the interplay between thermal fluctuations and interfacial energy in the liquid-to-solid transition of emulsions. We find a previously unknown elastic instability that makes emulsions susceptible to surprisingly small thermal perturbations, and describe some of its fascinating properties. We also investigate the effects of loading the interfaces of liquid droplets with solid nanoparticles; the dense packing solid particles on the droplet interfaces turns a soft and compliant material into a stiff yet fragile solid, whose Poisson's ratio may even become negative. Finally, we describe an application for the large specific surface area of polymer foams that improves the delivery poorly bioavailable pharmaceutical compounds. Here we dissolve hydrophobic drugs in a polymer melt and use the open, porous structure of a filled microcellular foam to quadruple the dissolution rate of active compounds over state-of-the-art formulations.

Contents

List of Figures

Acknowledgments

During my time in the Weitz lab I have been fortunate enough to meet and learn from an extraordinary number of people, certainly too many to list. The work described in this thesis represents results from three major projects that I was involved with, but does not cover all the work I was able to do and all the people that I was able to work with. Chapters 5 and 6 describe work that I was able to do together with Kosta Ladavac: were I took the lead on Pickering emulsions and he on foams. Chapters 2 through 4 describe work that I carried out mostly by myself, but does not include the exciting new results that have come from looking into questions raised by this research. Tom Kodger and I have developed a tremendous set of tools to let us explore the properties of liquid-like emulsions confined by extraordinary osmotic pressures using confocal microscopy – the results of which have lead me to reevaluate what I thought I had learned about glasses and amorphous solids.

To my family and friends

Chapter 1

Introduction and Summary

1.1 Thermodynamics of Emulsions

An emulsion is a collection of droplets of one liquid in another [6]. By diving one of the fluids into droplets we dramatically increase the interfacial area between them and must thus do work against their interfacial tension, σ. This work typically increases the free energy of the emulsion and makes such a material thermodynamically unstable. Droplet coalescence is the most striking mechanism that returns the fluid mixture to equilibrium, but this can be slowed or prevented by adding amphiphilic molecules, polymers, or solid particles that adsorb onto the interfaces: depicted schematically in Fig. 1.1. These surface active additives, so-called surfactants, reduce the interfacial tension between the fluids, but do not generally eliminate it. Instead, some surfactants can resist compression and prevent the surfaces of neighboring droplets from touching: thus trapping the fluids in a metastable configuration. The following chapters deal primarily with cases when the covered droplets interact weakly or not at all

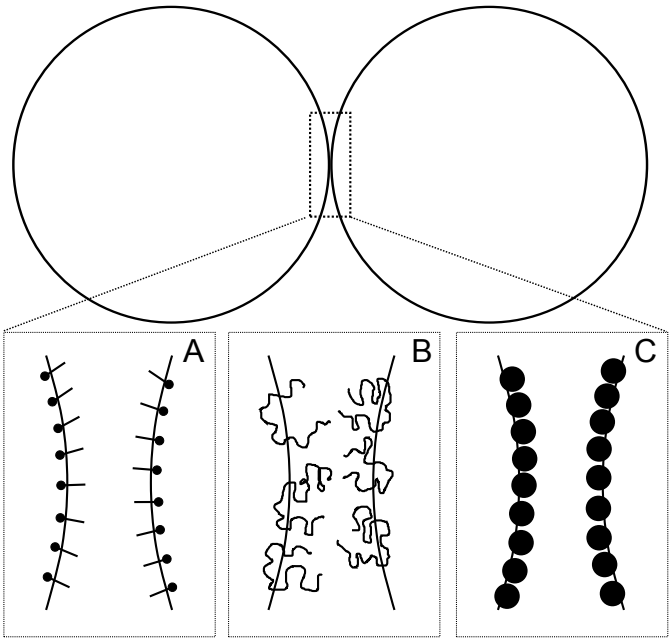

Figure 1.1: The surfaces of two adjacent droplets can be kept apart by adsorbed (A) amphiphilic molecules, (B) polymers, (C) solid particles.

unless they are forced together. This is usually the case when droplets are stabilized with simple detergents and the continuous phase does not contain other additives. Nevertheless it is possible to make droplets stick to each other quite strongly, without coalescing, by dissolving large quantities of salt or polymeric depletants in the continuous phase, or by choosing surfactants that undergo some chemical or physical transformation.

When the dispersed fluid has some, even if sparing, solubility in the continuous phase Ostwald ripening will also act to bring the fluids back to equilibrium. During this process molecules of the dispersed fluid diffuse through the continuous phase from smaller droplets to larger ones, reducing the total surface area of the emulsion. If this process is allowed to continue indefinitely, the smaller droplets become ever smaller and the larger ones grow larger until only one large drop remains. We can formulate

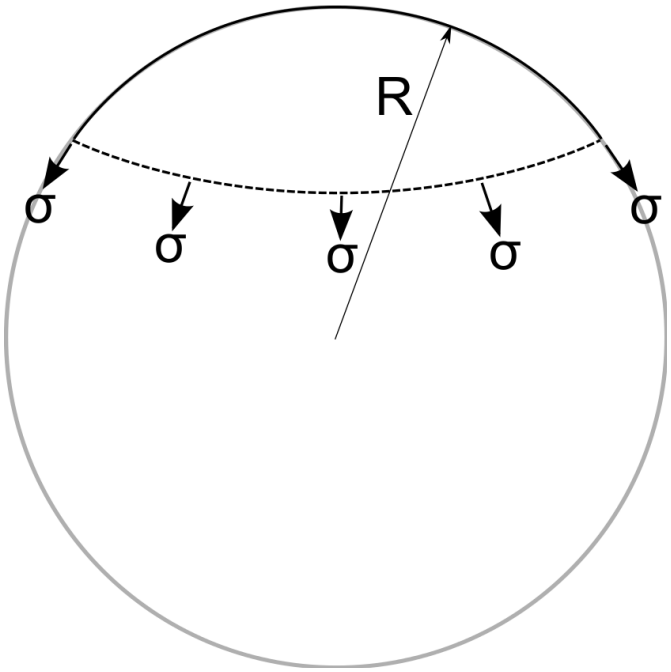

Figure 1.2: Interfacial tension pulling on a small patch of a sphere. The tangential force components are canceled by equal and opposite contributions by the remainder of the surface, but the unbalanced normal forces lead to a pressure equal to $\frac{2\sigma}{R}$.

an equivalent description of this process as pressure driven flow. As the tension of the interface pulls on every surface area element, any small patch of the surface of a sphere will have an unbalanced force that points radially inwards, proportional to the tension and the curvature of that patch: depicted schematically in Fig. 1.2. Integrating this force over the sphere leads to a pressure difference across the interface of $\frac{2\sigma}{R}$, called the Laplace pressure. The surface of a small droplet has a larger curvature than that of a larger one, the fluid inside smaller droplets thus exists at a higher relative pressure and so is osmotically driven to larger droplets.

For foams, emulsions of gas, this process cannot be stopped and leads to irreversible coarsening. However, if the dispersed fluid contains a material that is absolutely insoluble in the continuous phase this solute can exert an osmotic pressure that

pushes against that of the curvature. In this way, emulsions made of a fluid containing a dissolved polymer can be made stable against ripening as well a coalescence. This long term stability is essential to the kind of measurements described in the following chapters.

1.2 Packing Droplets

When the volume fraction, ϕ, of dispersed fluid is low the mechanical properties of the emulsion are essentially the same as those of an equal volume of pure fluid. Even at a volume fraction as high as 60%, droplets that do not stick to one another will only increase the viscosity of the emulsion moderately [22]. However, at some point it becomes impossible to pack the droplets further without forcing them to touch. When all the droplets are identical to one another it is possible to reach a volume fraction as high as $\frac{\pi}{3\sqrt{2}} \simeq 0.74$ by packing them into a regular crystal. Real emulsions are rarely so perfect, and an equivalent upper bound exists for disordered packings of droplets, called random close packing (RCP). Liquid droplets are nearly incompressible but are deformable, so it is still possible to pack them up to volume fractions close to 100%, but they must deform.

Compared to a sphere, any deformation of the droplet must increase its surface area: the total interfacial area of a compressed emulsion is then strictly larger than that of a more dilute one. This additional surface area directly increases the free energy of the emulsion and leads to a positive osmotic pressure. The thermodynamic drive to reduce the excess area also forces particles to rearrange until they find a sufficiently stable local minimum, and so small perturbations to this configuration

will be opposed by a linear response. Since the response to small perturbations of the shape of the container is elastic, a sufficiently concentrated dispersion of one fluid in another will act as a solid. The total free energy of this packing is proportional to the total surface area, so it is not surprising that the osmotic pressure and the elastic constants are proportional to the surface energy density, $\frac{\sigma}{R}$, but the dependence of these on the droplet concentration is not so obvious.

After spending twenty years studying the physical chemistry of bubbles, droplets, and films, Henry Princen spent much of the 1980s studying this problem [74–76]. Though the models he used to compare with his data were based on an oversimplified two dimensional construction, his investigations on the shear and bulk moduli, yield strain, and non-linear viscosity of emulsions helped define the field, and the experimental methods he developed are essentially the same as those used now. These results, along with subsequent ones from our lab and elsewhere, established that an emulsion remains fluid up to some critical volume fraction, ϕ_c, but that its osmotic pressure, Π, and shear modulus, G, increase as $\phi - \phi_c$ for small enough compressions [62, 75]. Because these quantities are essentially independent of temperature, even for sub-micron droplets, most of the theoretical work done to understand these measurements has assumed that the droplets may be treated as classical objects at zero temperature.

The first set of computer simulations that attempted to reproduce this behavior were based on this principle [47, 48]. Though this work showed that the forces exerted by droplets on their neighbors are not pairwise additive, this assumption, along with that of zero temperature, led to a series of interesting observations. First,

the authors found that the simulated droplets began to touch once the number of nearest neighbors was equal to six: the so-called isostatic condition. Beyond this point the average number of contacts per droplet increased as the square root of $\phi - \phi_c$. Second, they found that the ratio between the osmotic pressure and shear modulus, $\frac{\Pi}{G}$, scaled as $(\phi - \phi_c)^{1/2}$. This second observation, however, was at odds with the experimental results; nevertheless, large measurement noise and the difficulty of measuring samples at such small compressions made it difficult to compare these directly.

The last fifteen years have been dominated by the results of simulations not fundamentally different from these first ones. The lack of a strong temperature dependence of the elasticity and the qualitative similarity between the rheology of emulsions and microgels has led to a large body of work that has investigated not only the scaling of the linear moduli, but also the phonon density of states, flow rheology, elastic wave propagation, etc. The assumption that working at zero temperature is equivalent to modeling macroscopic, granular materials has motivated most of this work, but real granular materials have static frictional contacts which are much more difficult to simulate effectively.

1.3 Critical Elasticity of Emulsions

Predicting the macroscopic elasticity of compressed emulsions at arbitrary volume fractions is a challenging problem. However, a critical point at zero temperature and pressure is expected to dominate the mechanics at small compressions. Since theoretical predictions at infinitesimally small compressions disagree with extrapolations

of experimental data, we want to clarify the relationship between shear modulus and osmotic pressure at small compressions experimentally. To do this we have developed new sample preparation methods and measurement techniques. The results show that $\frac{\Pi}{G} \simeq const.$, in agreement with previous experimental results, and suggest that computer simulations of pairwise additive, soft repulsive spheres at zero temperature do not accurately capture the elastic behavior of emulsions: even very close to the liquid-to-solid transition.

The data also show that the shear modulus vanishes not a zero pressure, but at a pressure much larger than that required to vitrify a comparable hard sphere fluid. We identify this as the minimum pressure at which the packing is capable of withstanding the thermal agitation of its constituent drops. The core of our argument rests on the fact that not only does the shear modulus of the packing go down as the applied pressure is lowered, but so does the critical strain at which the material will yield. From the scaling of this yield strain with pressure we find that the energy density required to yield the material scales as $\Pi(\frac{\Pi R}{\sigma})^2$, so when $\Pi \ll \frac{\sigma}{R}$ it becomes feasible for $\frac{3\,K_B T}{4\,\pi R^3}$ to equal or exceed this energy density. A more perplexing observation is that, though the shear modulus seems to vanish abruptly, the variation of the density around this point appears continuous and probably smooth. We are not aware of another liquid-to-solid transition in three dimensions that shares this behavior. We are working to improve our understanding of this process by complementing our bulk measurements with microscopic particle trajectory data gathered using confocal microscopy and automated particle tracking.

Preparing a homogeneous emulsion at a volume fraction just barely above the

liquid-to-solid transitions remains a difficult problem. Simulations rarely consider compressions beyond $\phi - \phi_c \simeq 10^{-3}$, and this level of precision is nearly impossible to obtain in a bulk sample. However, trading ϕ for Π makes approaching this problem much easier. Droplets that are slightly denser than the continuous phase will settle into a vertical sediment that naturally has a linear pressure distribution starting from zero at the top of the packing. It is not easy to probe these piles mechanically, and samples prepared at very low osmotic pressures are too weak to be measured this way in the first place. Instead, we use light scattering and magnetic resonance imaging to measure the shear modulus and density of the packed droplets as functions of height, and therefore pressure. These measurements required several experimental innovations that will be described in the following chapters.

1.4 Elasticity of Pickering Emulsions

While the work described in the previous section is most relevant to emulsions stabilized by molecules as those depicted in Fig. 1.1A, solid particles are also effective emulsifiers [71, 77] and have a dramatic effect on the mechanical properties of the resulting emulsions [2, 11, 50]. Such solid particles can be found in the casein proteins that stabilize the droplets of fat in homogenized milk, the sand and clay particles that stabilize emulsions of crude oil extracted from the ground, the particles of metal ore coating bubbles of gas formed during the flotation step of metal refinement, and the algal debris that stabilizes sea froth. These kinds of foams and emulsions were first described by Pickering and Ramsden, and several experimental studies have shown that the shear elastic modulus of emulsions stabilized by solid particles can be an

order of magnitude larger than that of an equivalent emulsion stabilized by small molecules. The reason for this enhancement is not clear, and preparing a particle stabilized emulsion that faithfully reflects the diagrammatic depiction of Fig. 1.1C is not straightforward. When the particles that stabilize the liquid interfaces stick to one another it is difficult to prepare interfaces coated with particle monolayers and to prevent droplet surfaces from sticking to one another as well.

We designed a Pickering emulsion system that has a critical onset of elasticity like that of emulsions stabilized by molecular surfactants. The particles that stabilize these droplets do not stick strongly to one another and do not lead to the aggregation of the droplets that they stabilize. This new formulation has allowed us to better study the mechanical properties of these emulsions. Without strong droplet-droplet adhesion it becomes possible to measure the bulk modulus of a quiescent emulsion compressed by its own weight. Using conventional oscillatory rheology we still find that the shear elasticity of these emulsions is an order of magnitude larger than that of an equivalent system of surfactant stabilized droplets, but x-ray densitometry measurements show that the bulk modulus is not.

What is perhaps most intriguing about the particle stabilized system is that it is so similar to the surfactant stabilized case, yet different. Isotropic deformations increase the surface area of the droplets, and so the particles bound to the interface will have more free surface and so a lower surface pressure. Therefore it is plausible that the work done to compress a Pickering emulsion is done against the interfacial tension – as is the case with their surfactant stabilized counterparts – which may explain why their bulk moduli are similar. However, that the shear modulus is an order of

magnitude larger and has no meaningful frequency dependence implies that the bound particles form long lived structures that resist this deformation. A simple elastic shell model predicts that the shear modulus should not scale as the inverse droplet radius alone, but this prediction is not correct. Moreover, it seems like the yield stress of a particle stabilized emulsion is nearly identical to that of an equivalent surfactant-stabilized system. These observations are difficult to reconcile with the idea that the liquid-to-solid transition of emulsions is controlled by some simple, universal critical point.

1.5 Pharmaceutical Applications of Polymeric Foams

Close to 40% of newly developed pharmaceutical compounds are poorly water soluble. This hydrophobicity slows down their dissolution in the digestive tract and makes it difficult for these compounds to enter the blood stream quickly and effectively [4, 28]. It is possible to improve the dissolution rate of these compounds by formulating them as nanoparticles with large surface to volume ratios [36, 64, 66, 80]. Doing so requires using procedures that are either compound specific or energy intensive. However, it is quite simple to produce polymer foams that have equally large surface to volume ratios using rapidly depressurized supercritical CO_2 to blow the bubbles. Moreover, some of the low molecular weight polymers that are already approved as pharmaceutical excipients can be processed in this way without affecting their pharmaceutical safety[3, 41, 85].

Like emulsions, closed-cell foams are composed of large bubbles that are separated by films of the continuous phase. This collection of bubbles can also be compressed,

and the space between the bubbles can be squeezed down to be one to two orders of magnitude smaller than the bubbles themselves. Once the volume fraction of gas reaches $\sim 90\%$ the surface to volume ratio of the continuous phase is an order of magnitude greater than that of the bubbles. By blowing micron sized bubbles into a polymer matrix that contained dissolved pharmaceutical actives we were able to produce powders that released this active twice as fast as the state-of-the-art formulation.

The demixing of the gas drives a rapid expansion of the polymer followed by the irreversible quenching of the porous structure. This process is far from equilibrium and so these foams need not obey any surface area minimization principle; yet it is still true that the space between three or more bubbles is much larger than the film separating two adjacent bubbles. We found that solid particles mixed into the polymer matrix before foaming would collect in these Plateau borders if they were much larger than the typical film thickness. These particles act as inert inclusions that push material out of the thickest regions of the foam without affecting the gross morphology or pharmaceutical acceptability of the resulting foam. Surprisingly, foams made by blowing a polymer blended with 25 vol. % silica particles could be milled into powders that released their active four times as fast as the original formulation.

Chapter 2

Entropic Unjamming of Emulsions

An externally applied osmotic pressure, Π, can turn a viscous dispersion of fluid droplets into an elastic solid; as the applied pressure drains the surrounding fluid, droplets stabilized by surfactants are forced to pack, deform, and jam into a disordered structure that responds elastically to small strains [62, 75]. Deformations of the bulk material are translated into deformations of the droplet interfaces, which store elastic energy, and the elastic constants of the compressed emulsion are thus proportional to the ratio of the interfacial tension between the fluids and droplet radius: $\frac{\sigma}{R}$ [60]. This interfacial energy density is typically 10^6 to 10^{10} times greater than the thermal energy density of droplets, and strongly compressed emulsions can be exceptionally strong materials. Yet, as the confining pressure decreases, the forces that hold droplets in place weaken, and packings made from purely repulsive droplets become ever softer and more fragile. As the material softens, thermal fluctuations become increasingly important and could be critical to the fluid-to-solid transition of this amorphous material: a process that remains poorly understood.

Here we show that the mechanical properties of compressed emulsions change dramatically around a critical osmotic pressure, Π^*, below which the solid is too weak to resist the thermal excitations of its constituent droplets. For emulsions were the ratio between surface and thermal energy densities is $\sim 10^8$, Π^* is $\sim 10^5$ times larger than $\frac{3\,k_B T}{4\pi R^3}$, and separates solid-like from fluid-like behavior. Diffusing wave spectroscopy (DWS) measurements of emulsions confined by pressures lower than Π^* show a two-step relaxation like that of supercooled fluids; yet, emulsions confined by pressures higher than Π^* appear elastic. Similarly, magnetic resonance tomography (MRT) measurements show that the volume fraction of the emulsion increases rapidly yet smoothly below Π^*; the bulk modulus thus changes by an order of magnitude, but does not appear discontinuous.

We prepare an aqueous emulsion of monodisperse oil droplets stabilized with 2mM sodium dodecylbenzenesulfonate (SDBS) by swelling $4.2\,\mu$m diameter particles of linear polystyrene [42, 51, 67] with anisole to a final diameter of $7.2\,\mu$m. We do not measure the interfacial tension of the droplets directly, but estimate that $\sigma \simeq$ 5mN/m by measuring the interfacial tension of polystyrene-anisole mixtures using a ring tensiometer (Sigma 700, KSV) [37, 38]. The surface energy density of this emulsion, $\frac{\sigma}{R} = 1400\,\text{Pa}$, is $\sim 10^8$ times larger than its thermal energy density, $\frac{3\,k_B T}{4\pi R^3} = 16\,\mu\text{Pa}$. We load these droplets in a rectangular tube and allow them to settle, replacing the clear supernatant with additional emulsion, until the sediment is 20 cm tall. Lacking frictional contacts with the glass walls, the sediment slowly consolidates and reaches mechanical equilibrium once every horizontal slice of emulsion bears the weight of all the material above it [8, 70, 81]. This gravitational stress pushes droplets

closer together, but the difference in volume fraction between the top and bottom of the sediment is small when the stress is much smaller than $\frac{\sigma}{R}$. For such small applied pressures, the gravitational stress thus increases nearly linearly with depth below the free surface, d, and sets the local $\Pi(d)$ and droplet volume fraction, $\phi(d)$.

The large difference between the refractive indexes of the water and oil make this emulsion opaque. Laser light incident on the emulsion is scattered by the droplet interfaces and photons typically interact with dozens of interfaces before exiting the emulsion. Backscattered photons thus acquire random phases and momenta during their transit, and their interference produces a random speckle pattern [21, 52, 79, 88]. The thermal agitation of droplets leads to fluctuations in their positions and nanometer scale fluttering of their interfaces. These displacements alter the paths of photons and cause fluctuations in their accumulated phases; because every photon interacts with so many droplets, phase shifts induced by individual nanometer scale displacements accumulate and can cause the flickering of interference speckles. These intensity fluctuations thus encode underlying droplet motions, and the temporal correlations of these intensity fluctuations reflect the ensemble averaged droplet mobility [27, 58, 61, 93]. The multiple scattering condition also limits the distance photons travel within the material, and limits the sampled volume to be a few millimeters deep and a few millimeters wider than the illumination spot. This spatial selectivity makes it possible to sample the droplet mobility at different sediment depths and pressures well below 1 Pa.

To measure the time and pressure dependence of these intensity fluctuations we mount the sedimented sample on a vertical translation stage, illuminate it with a 1 cm

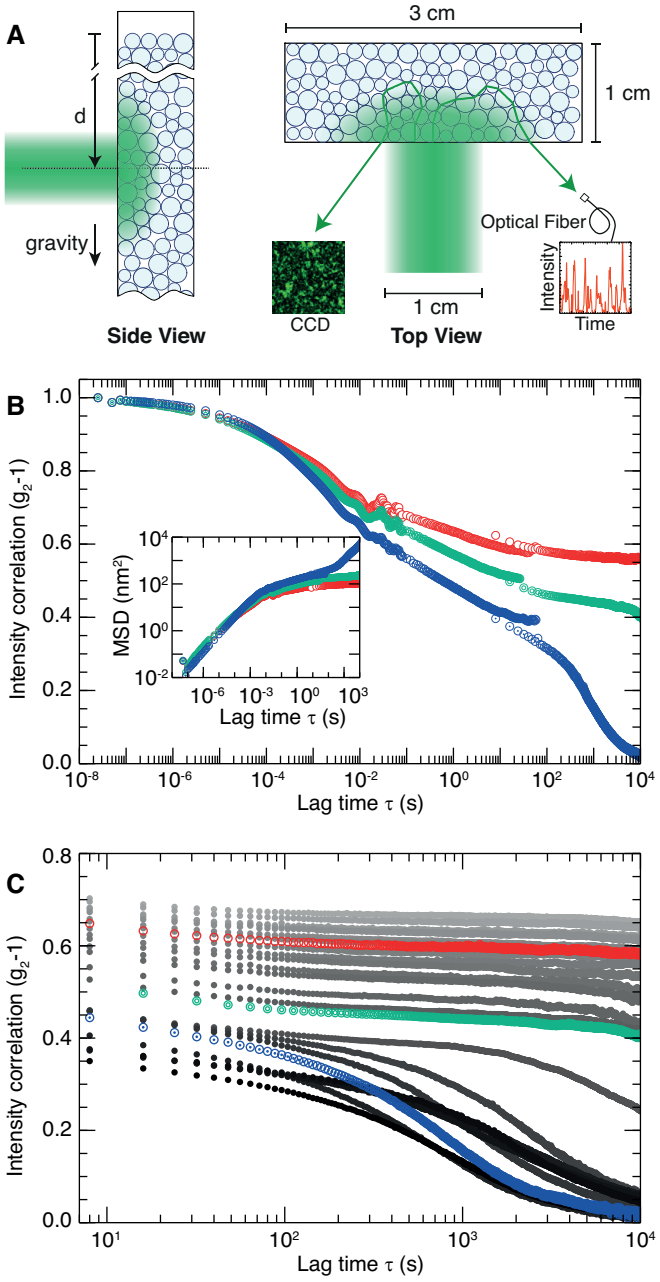

Figure 2.1: (A) Schematic of diffuse backscattering instrument. (b) Backscattered laser light intensity autocorrelations measured 1.3 cm (blue), 4.9 cm (green), and 8.5 cm (red) below the top of a sedimented emulsion sample held at 31.5°C. (B) Intensity correlations for this sample measured at increasing depths.

diameter, linearly polarized laser beam, and collect cross-polarized, backscattered light using camera (Retiga EXL, Qimaging, 63 μs exposure time) and a split single-mode fiber, as depicted schematically in Fig. 2.1A [7, 59, 78, 94]. The intensity of the light collected by the fiber is recorded by two avalanche photodiodes (SPCM-AQRH, Perkin-Elmer) and cross-correlated by a hardware correlator (BI-9000AT, Brookhaven Instruments Corporation). This correlator computes $g_2(\tau) = \frac{\langle I(t+\tau)I(t)\rangle}{\langle I(t)\rangle\langle I(t+\tau)\rangle}$, for lag-times, τ, between 50 ns and 90 s. Meanwhile, the camera records snapshots of the scattered light intensity every few seconds. These images are cross-correlated by a computer and used to extend the domain of $g_2(\tau)$ to several hours [90]. The intensity correlations obtained by combining the data gathered from both detectors span twelve orders of magnitude in time, and extend to much longer lag times than have been accessible before. The full time dependence of $g_2(\tau)$ measured 1.3 cm, 4.9 cm, and 8.5 cm below the top of a sedimented are shown in Fig. 2.1B.

The form and progression of the intensity autocorrelations measured at these different depths into the sediment, d, resemble those of a glass forming liquid measured above and below its glass transition temperature. For $\tau \lesssim 100$ s, all correlations show a monotonic decay reminiscent of the β relaxation of glassy materials. This decay is universal feature of glass formers, and reflects the hindered rattling of scatterers within a cage formed by their neighbors [43, 44]. However, for $\tau \gtrsim 100$ s, intensity correlations measured beyond a critical depth, d^*, into the sediment are qualitatively different from those gathered below it. Correlations measured at depths beyond d^* reach a stable plateau value that increases with increasing depth, consistent with increasing, solid-like elastic moduli [30, 61]. By contrast, the intensity correlation

measured closest to the top of the sediment shows an additional decay at longer times reminiscent of the cage-breaking, α relaxation of supercooled fluids [10, 12, 63]. This second decay is best captured in the data gathered from the cross-correlated images, and we plot the data gathered at increasing depths into a sediment equilibrated at 31.5°C in Fig. 2.1C. The size of our laser spot limits how finely we can resolve the depth dependence of $g_2(\tau)$; nevertheless the data show a clear separation between fluid-like and solid-like behavior at a d^* that lies between 3 cm and 4 cm below the top of the sediment .

We represent the depth and long time behavior of these intensity correlations more compactly by converting the long time plateau of each $g_2(\tau)$ into a corresponding low frequency shear modulus, G, using DWS microrheology. Microrheology relates the microscopic fluctuations in the positions of droplets to the macroscopic shear modulus through the equipartition relation of elastic energy [56]: $G = \frac{k_B T}{\pi \langle \Delta r^2 \rangle R}$, where $\langle \Delta r^2 \rangle$ is the mean squared displacement of droplet centers. DWS microrheology provides a way to compute $\langle \Delta r(\tau)^2 \rangle$ from $g_2(\tau)$ when the diffusely scattered photons can be assumed to follow a random walk within the material [58, 61, 93]. We thus compute a low frequency shear modulus at each height by approximating $g_2(\tau)$ by its value measured at 10^4 s (Chapter 3). By plotting the data in this way it becomes apparent that G is proportional to the depth for $d > d^* \simeq 4$ cm, but that it drops abruptly below this, as shown in Fig. 2.2A.

Though our depth selective measurements allow us to determine d^*, this fluid-to-solid transition should instead be controlled by a critical pressure, Π^*. These two quantities are connected through an applied pressure gradient that we can change

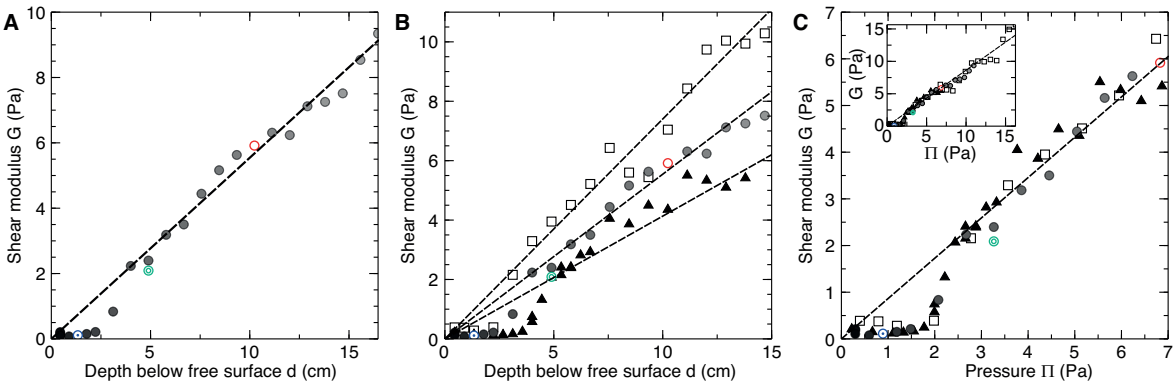

Figure 2.2: (A) Shear moduli inferred from the plateau value of intensity correlations collected at increasing depths below sediment surface from sample held at 31.5°C. Dashed line is a guide for the eye. (B) Shear moduli measured for samples held at 27°C, 31.5°C, and 34.9°C, plotted against sediment depth. (C) Shear moduli measured for samples held at 27°C, 31.5°C, and 34.9°C, plotted against sediment pressure. Inset. Expanded range of shear moduli and pressures.

by manipulating the slight density difference between the oil and the surrounding water. We use the much larger thermal expansion coefficient of the oil to vary this gradient by a factor of two, and repeat our light scattering measurements at 27.0°C and 34.9°C without affecting the stability of the emulsion or interfacial tension. We plot the depth dependence of the shear moduli obtained by converting the plateau values of intensity correlations gathered at each temperature depth in Fig. 2.2B. The data show that both d^* and the proportionality constant between d and G at large depths depend on temperature; however, this dependence should vanish if we compute $\Pi(d)$ and plot $G(\Pi)$ instead.

To approximate $\Pi(d) = g\,\delta\rho\,\int_0^d \phi(z)\,\mathrm{d}z$ we measure the density difference between the two fluids, $\delta\rho$, but assume that the variation in the volume fraction of the column with depth is much smaller than $\phi(d=0) = \phi_c$. From the sedimentation velocity of the droplets [65] and the thermal expansion coefficient of anisole [33] we estimate

that the density differences between the oil and water at 27°C, 31.5°C, and 34.9°C are $14\,\mathrm{kg/m^3}$, $11\,\mathrm{kg/m^3}$, and $8\,\mathrm{kg/m^3}$ respectively. We also assume that ϕ_c is not significantly different from the random close packing volume fraction of monodisperse spheres, $\phi_{RCP} \simeq 0.635$. We use these estimated values of $\Pi(d)$ to eliminate the explicit depth dependence from $G(d)$, and plot the pressure dependence of the shear moduli in Fig. 2.2C. The resulting plots of $G(\Pi)$ collapse almost perfectly, and suggest that the elasticity of our emulsion vanishes below a critical pressure $\Pi^*_G \simeq 2.5\,\mathrm{Pa}$. The magnitude of this critical pressure is surprisingly large. By comparison, Π^*_G is $\gtrsim 10^5$ larger than the thermal energy density of this emulsion, $\frac{3\,k_B T}{4\,\pi R^3} \simeq 16\,\mu\mathrm{Pa}$. A comparable hard sphere fluid would be expected to solidify well below 1 mPa [5]. The soft repulsion between the droplets thus dramatically changes the character of their fluid-to-solid transition.

Instead of addressing the solidification of the fluid-like sediment it may be possible to understand this transition as a mechanical instability of the solid. Since the data presented in Fig. 2.2C suggest that $\Pi \sim G$ in the solid phase, we can estimate the typical distance a droplet confined in an elastic packing may diffuse away from its equilibrium position by replacing G with Π in the elastic equipartition relation:

$$\langle \Delta r^2 \rangle = \frac{k_B\,T}{\pi\,\Pi\,R} \tag{2.1}$$

For vanishingly small pressures, (2.1) suggests that droplets could diffuse many times their own size before finding their way back to their equilibrium positions. However, such long excursions taken by all the droplets simultaneously should destroy the network of bonds that hold them in place. In particular, if all the droplets that compose the emulsion can move far enough to locally yield their surroundings it should

not be possible to maintain a stable solid. We thus propose that Π^* corresponds to the pressure where $\sqrt{\langle \Delta r^2 \rangle}$ is equal to $2\,R\,\gamma_y(\Pi)$, where $\gamma_y(\Pi)$ is the macroscopic, pressure dependent yield strain of the emulsion.

Previous experimental studies have shown that the yield strain scales linearly with the excess volume fraction, $\delta\phi = \phi - \phi_c$, as does G. We use the following empirical scaling relations [82] to estimate our critical confining pressure, Π^*:

$$\begin{aligned} \gamma_y(\phi) &= \frac{\phi - \phi_c}{2} \\ G(\phi) &= \frac{\sigma}{R}\phi(\phi - \phi_c) \\ \Pi &= G \end{aligned} \tag{2.2}$$

By assuming that $\phi \simeq \phi_c$ near the transition we can eliminate the volume fraction dependence entirely and recast eq. 2.1 in terms of Π, R, and σ:

$$\left(2\,R\,\gamma_y(\Pi^*)\right)^2 = \left(\frac{\Pi^*\,R^2}{\phi_c\,\sigma}\right)^2 = \frac{k_B\,T}{\pi\,\Pi^* R} \tag{2.3}$$

By defining an energy density $\epsilon = \frac{\sigma}{R}$ and a reduced temperature $\bar{T} = \frac{k_B\,T}{4\pi\sigma R^2}$ we can simplify eq. 2.3 further:

$$\Pi^* = \left(\frac{k_B\,T\phi_c^2\sigma^2}{\pi\,R^5}\right)^{\frac{1}{3}} = \epsilon\,\bar{T}^{\frac{1}{3}}\,(4\phi_c^2)^{\frac{1}{3}} \simeq \epsilon\,\bar{T}^{\frac{1}{3}} \tag{2.4}$$

For this emulsion $\epsilon \simeq 1400\,\text{Pa}$ and $\bar{T} \simeq 5 \cdot 10^{-9}$. Evaluating eq. 2.4 with these values yields $\Pi^* \simeq 2.8\,\text{Pa}$, which is in remarkably close agreement with the measured value of Π^*_G.

Though this thermally induced yielding process provides an intuitive explanation for the precipitous drop in G below Π^*_G, it is not obvious how it will affect the compressibility of the emulsion. In particular, the abrupt drop in G could be accompanied

by a concomitant drop in the droplet volume fraction, ϕ, or a discontinuity in the bulk modulus. To measure $\phi(\Pi)$ we program a high field nuclear magnetic resonance (NMR) spectrometer to measure the density of a sedimented emulsion tomographically. A pulsed field gradient coil applies a nearly constant magnetic field gradient parallel to $\vec{g}$ that shifts the resonant frequency of protons based on their depth. A simultaneous gradient and spin echo pulse sequence then produces a short burst in the current induced in a detector coil when the phase of the precessing spins is refocused [15, 72, 73, 86] (Fig. 2.3A). From the power spectrum of this burst we infer the proton density at every measured frequency, and thus depth. The resolution of this kind of tomography is best when all the spins are chemically identical, so we prepare 13.2 μm diameter, monodisperse droplets of 20 cst silicone oil and tetrachloroethylene stabilized in D_2O with 2 mM SDBS [16, 91]. These droplets are then loaded into a 5 mm NMR tube and allowed to equilibrate for several days (Chapter4).

From the measured density profile it appears that $\frac{d\phi}{dh}$ is nearly constant deep into the sediment, but there is a clear deviation close to the top that appears continuous and smooth (Fig. 2.3B Inset). The density difference between the oil and water is $\simeq 150 \mathrm{kg/m^2}$ so we convert these data into a measurement of $\phi(\Pi)$. By fitting $\phi(\Pi > 4\,\mathrm{Pa})$ to $\phi(\Pi) = \phi_c + \frac{\Pi}{\epsilon\,\phi_c}$ we extract a value for ϵ of 340 Pa that corresponds to a water-oil interfacial tension of $\sigma = 2.3\,\mathrm{mN/m}$. This value for σ is only slightly lower than the value measured for a comparable solution using a ring tensiometer. $\phi(\Pi)$ near the top of the sediment also appears to increase linearly, and the cross-over point between these linear extrapolations occurs at $\Pi^*_\phi \sim 0.7\,\mathrm{Pa}$. The slope of $\phi(\Pi)$ at low pressure also suggests that the bulk modulus decreases tenfold compared to

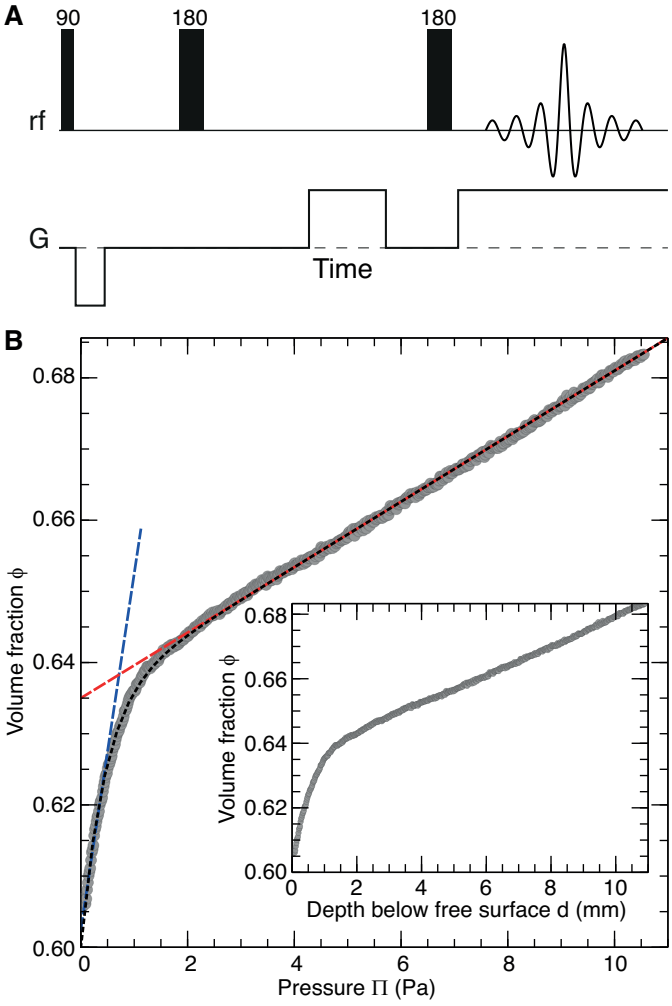

Figure 2.3: (A) Spin and gradient echo pulse sequence. (B) Height dependence of oil volume fraction measured with MRT. Inset. $\phi(\Pi)$ as determined in the text. The dashed red line is a line proportional to $\frac{\Pi}{\phi_c \epsilon}$. The dashed blue line is a linear fit to $\phi(\Pi)$ for small pressures. The dashed black curve is fit described in eq. 2.5 using Π^*_ϕ value of 0.45 Pa.

$\Pi > 4\,\mathrm{Pa}$ (Fig. 2.3B)

Despite having a lower interfacial tension than the anisole/polystyrene droplets, the larger droplet size lowers the reduced temperature to $\bar{T} \simeq 3.3 \cdot 10^{-9}$ and the thermal energy density to $3.4\,\mu$Pa. From (2.4) we estimate $\Pi^* \simeq 0.6\,\mathrm{Pa}$, which again is $\gtrsim 10^5$ times larger than $\frac{3\,k_B T}{4\,\pi R^3}$, and agrees remarkably well with Π^*_ϕ. The data do not show any abrupt change in the density in this region, and the entire density profile can be well approximated by:

$$\phi(\Pi) = \phi_c + \frac{\Pi}{\epsilon\,\phi_c} - \delta\phi\,\exp\left(-\frac{\Pi}{\Pi^*_\phi}\right) \tag{2.5}$$

Having fit ϵ previously, we find $\delta\phi = 0.035$ and $\Pi^*_\phi = 0.45$ (Fig. 2.3).

These results demonstrate the importance of thermal fluctuations to the fluid-to-solid transition of emulsions. The softness and fragility of weakly compressed emulsions provides a mechanism whereby the thermal fluctuations of droplets can continually yield and restructure their environment: despite confining pressures 10^5 times larger than $\frac{3\,k_B T}{4\,\pi R^3}$. A simple estimate for the confining pressure below which the solid becomes unstable agrees with the fluid-solid boundary found from light scattering measurements, and points to a region of the equation of state where the bulk modulus of the emulsion rapidly, but continuously, changes by a factor of 10. The combination of an abrupt drop in the shear rigidity with a smoothly decreasing density makes this unjamming transition quite unique. We believe that an elastic instability of this kind is an inescapable consequence of the increasing softness and fragility of jammed materials at low pressures, and should thus be a universal property of such soft-solids.

Chapter 3

Diffusing Wave Spectroscopy of Nearly Athermal Emulsions

The interference pattern of laser light multiply scattered from a turbid solution is extraordinarily sensitive to small changes in the position and optical properties of the objects from which it scatters. As a photon travels through a turbid medium it is deflected again and again: the tortuousity of the path it traces before exiting the material effectively randomizes its momentum and phase. The intensity distribution of the speckle pattern created by the interference of photons following many such paths encodes information about the instantaneous position of these scatterers, and the time dependence of the speckle intensities can be used to infer dynamical information about the scatterers themselves: including sub-nanometer displacements and small variations of their refractive index.

This sensitivity makes multiply scattered light ideally suited to measure the mobility of the particles that compose soft solids: such as dense emulsions and glassy

colloidal dispersions. The generalized Stokes-Einstein relation (GSER) connects the mobility of the individual particles to the viscoelastic properties of the bulk, and thus provides a non-invasive way to measure their elasticity. However, the sensitivity of the interference pattern and the slow, metastable dynamics of these materials makes these measurements susceptible to drift and noise. Small changes in the frequency spectrum of the laser light and small changes in the refractive index of the scatterers are amplified by the wide distribution of photon path lengths. A slowly drifting temperature can lead to irreversible rearrangements in soft materials which are close to structural transitions. These rearrangements cause intermittent "avalanches" in the speckle intensity correlations that do not reflect the stationary behavior of the material. Nevertheless, many of these materials are too weak or history dependent to probe mechanically, and overcoming these obstacles is essential to produce accurate measurements.

Here we show that it possible to use diffuse reflectance to measure nanometer scale displacements in soft, elastic materials over several hours; we use multi-speckle diffusing wave spectroscopy (DWS) to study the aging dynamics of a compressed emulsion and measure the pressure dependence of the shear modulus of a quiescent emulsion sample. We obtain intensity autocorrelations spanning several hours reproducibly when fluctuations in the temperature of the sample and the laser cavity are kept below 0.01°C, and when the effects of vibrations and slight mechanical perturbations are compensated for.

3.1 Synthesis of Monodisperse Emulsions

We prepare monodisperse emulsions of oil in water by swelling particles of linear polystyrene, made using a multi-step seeded dispersion polymerization process dispersed in a 2 mM solution of sodium dodecylbenzene sulfonate (SDBS), with anisole. We prepare the micrometer sized seeds by dispersion polymerization of 10 volume % styrene in ethanol, with 1.6 grams of polyvinyl pyrolidone (Kollidon 30 BASF) stabilizer per hundred milliliters of liquid and 1 wt. % azobisisobutyronitrile (AIBN) to styrene. We mix all the reagents in a round-bottom flask, degas, evacuate, and seal them. We then place the flask in an oil bath held at 70°C and rotate it at a constant rate of a few tens of RPM to provide gentle mixing. We wash these seed particles by repeatedly centrifuging and resuspending them in pure ethanol. We then add these seed particles to a solution similar to the one described above but with up to 40 vol. % styrene, azobis(cyanocyclohexane) (ACHN) and 0.5 wt. % octanethiol to styrene. The thiol reduces the average molecular weight of the new polymers, and thus reduces the viscosity of the final oil droplet, but interferes with the nucleation process of the particles. By seeding the reaction with monodisperse particles much smaller than the final target size and using the more slowly decomposing ACHN radical initiator we avoid nucleating new particles and produce larger, monodisperse spheres with lower molecular weight. We improve the uniformity of the resulting particles by splitting the total volume growth into three separate growth steps, and prepare 4.2 μm diameter particles composed mostly of low molecular weight polymer.

After washing these particles with ethanol several times, we resuspend them in a 2 mM solution of SDBS and expose them to anisole. The low molecular weight

polymer chains provide enough osmotic pressure to swell the particles many times their starting volume, but we choose to swell them to a final diameter of 7.2 μm. At this polymer/solvent composition the dilute sedimentation velocity is approximately 2 mm/hr, from which we estimate a density difference of 20 kg/m^3 between the oil and water.

3.2 Sediment Formation and Equillibration

The effective transport mean free path, l^*, for light traveling in a compressed emulsion made from these droplets is $\sim 100\,\mu$m. To minimize the amount of light transmitted through the sample we hold the emulsion in 1 cm thick tubes. The dimensions of the illuminated area must also be many times larger than l^*, so we expand the laser beam to a 1 cm diameter and use tubes that are at least 3 cm wide. For our quiescent sample we build a 20 cm tall sediment of liquid droplets by allowing a 10 vol. % dispersion of droplets to settle inside a rectangular glass tube. The Peclet number of these droplets is greater than 50, and crystallization of the droplets is not expected even at much lower sedimentation density. We accelerate the sedimentation rate further by tilting the column at a slight angle. As the droplets settle we replace the clear supernatant with more droplet dispersion twice per day until the sediment reaches its final height, and seal the top of the tube with a glass plate and epoxy resin. After the sample is sealed we allow the sediment to slowly consolidate at room temperature for six months.

We transfer the emulsion column into the thermostatted box several months before performing any measurements and securely mount it on a plate fixed to a vertical

translation stage with approximately 30 cm travel. We control the temperature inside the box by forcing air over a Peltier plate that is controlled by an electronic thermostat (TED200, Thorlabs). We control the temperature of the bottom plate of the illuminating laser (Compass 315M-50, Coherent Inc.) using a feedback controlled Peltier plate. The back side of both Peltier plates are attached to heat blocks that are constantly flushed by a temperature controlled water recirculator. The resonant cavity of the laser is cemented onto the bottom plate of the device, so careful thermostatting of this element provides sufficient stabilization of the carrier frequency for the duration of each measurement. We record the temperature at the bottom plate of the laser and of the air temperature inside the box. We find that the typical variation of the temperature inside the sample chamber during a 20 hour measurement is less than $\pm 0.01°\mathrm{C}$ and that the typical variation of the temperature of the bottom plate of the laser is below our measurement noise floor of $\pm 0.001°\mathrm{C}$.

3.3 Design of Light Scattering Apparatus

The suitability of different modes of scattered light spectroscopy depends on the magnitude and timescale of the scatterer displacements. To determine the low frequency mobility of the droplets we need to measure the plateau root mean squared displacement (RMSD) of the droplets. We use the equipartition of thermal energy relation for a bead embedded in an elastic solid to estimate the order of magnitude of this RMSD:

$$\langle \Delta r^2 \rangle \sim \frac{k_B T}{\pi R G}$$

where G is shear modulus of the solid, and R is the radius of the embedded particle. For droplets several micrometers in diameter embedded in an elastic material with a shear modulus of a few Pa, we can expect RMSDs of a few tens of nanometers. This displacement is too small to accurately resolve using optical microscopy or single light scattering, but is also too large to resolve with transmitted light DWS. Instead, we perform our measurements using the diffusely backscattered light were we can resolve RMSDs of up to 50 nm.

For lag times below a few tens of seconds, a hardware correlator (BI-9000AT, Brookhaven Instruments Corporation) cross-correlates the intensity collected by a split, single-mode, fiber optic attached to two avalanche photodiodes (SPCM-AQRH, Perkin-Elmer). The light detected by both detectors is collected from the same point, so the cross-correlated signal is statistically equivalent to the auto-correlated. By splitting the light onto two detectors we reduce the signal intensity, but remove the effects of correlated detector noise and shot noise statistics. To obtain averages over a large enough ensemble of independent speckles we sample over hundreds of speckles by rotating an acrylic disk that is placed at an oblique angle to the optical axis of the fiber. Temporal autocorrelations of the intensity for longer lag times are computed from snapshots taken with a CCD camera (Retiga EXL, Qimaging, 63 μs exposure time). The effects of mechanical drift and vibrations on the data gathered with the camera can be compensated by computing spatial as well as temporal autocorrelations of the speckle pattern intensity.

For the assumptions that underly DWS microrheology to be valid the photons that arrive at the detector must have undergone diffusive random walks within the

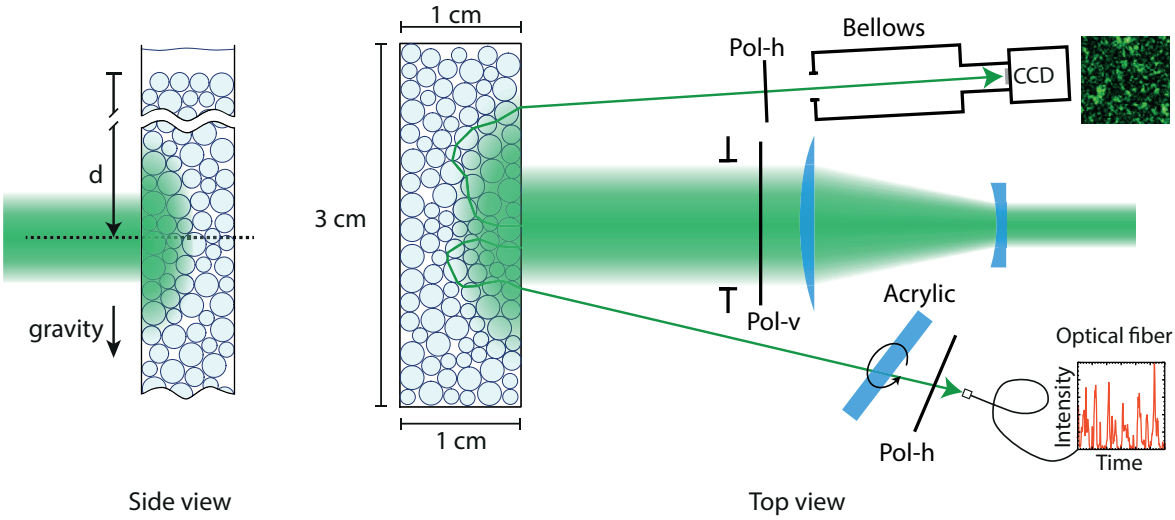

Figure 3.1: Schematic representation of DWS apparatus. The emulsion is illuminated from one side with a 1 cm diameter, vertically polarized laser beam. Horizontally polarized light reflected by the sample is collected by a single mode fiber and a CCD detector. An acrylic disk is placed in front of the fiber and rotated at an oblique angle to refract the incident light.

sample; yet, diffusely reflected light includes paths as short as single reflections off the surface of the material. However, because the typical path length over which the polarization of a photon is randomized, l_p, in this material is comparable to l^*, we exclude paths shorter than l^* when we illuminate the sample with vertically polarized light and collect the horizontally polarized backscattered light. Moreover, since l^* is over ten times larger than the diameter of a single particle, even photons that follow paths as short as a single l^* interact with many droplets before they exit the material. A simplified schematic of our instrument can be seen in Fig. 3.1.

Scatterers embedded in an elastic medium have RMSDs that plateau to a finite value. This localization restricts the variation in the phase acquired by the scattered photons and leads to speckle patterns that are not ergodic. Proper ensemble averaging then requires sampling many statistically independent speckles. For large,

area resolved detectors such as our CCD the solution to this problem is straightforward. For detector placed far from the illuminated sample, the size of the speckles is determined by the van Cittert-Zernike theorem:

$$d \sim \frac{\lambda\, z}{D}$$

were d is the spatial correlation length of quasi-monochromatic light of wavelength λ measured a distance z away from an incoherent source of size D. Though the spatial correlation length of light at the surface of the emulsion is larger than λ, neighboring speckles will be statistically independent when the illuminated area is sufficiently large. The speckle correlation size and shape can be measured from spatial correlations of gathered frames; however, because of the finite area of CCD pixels, the recorded intensity reflects a spatial average of the local intensity.

Uniformly illuminated frames should have a single peak at the origin standing on a perfectly flat background. We adjust the distance of the camera to make the correlated area of each speckle comparable to that of ten pixels: this provides approximately 150,000 independent speckles per snapshot. The pixel size is still comparable to the spatial correlation length of the speckle pattern, so the $\tau \to 0$ limit of the intensity-intensity autocorrelation, $g_2(\tau) = \frac{\langle I(t)\, I(t+\tau)\rangle}{\langle I(t)\rangle^2}$, is not exactly 2, but lies between 1.7 and 1.8. When pixel noise or shot noise are significant, frame auto-correlations will have an additional, delta-correlated peak at zero displacement corresponding to the variance of this noise: cross-correlations between different frames will not show this feature. Stray light and reflections can distort the baseline and can add an uncontrolled heterodyne components to the collected interference pattern. We eliminate these by placing an absorptive bellows in front of the CCD, as depicted in the schematic Fig. 3.1.

The position and shape of the correlation peak reflects the effects of mechanical drift and vibrations. Peaks from auto-correlated frames gathered with a sufficiently short exposure time are not smeared or distorted by motion averaging, but such motions are reflected in cross-correlated frames as displacements of the centroid. We fit the correlation peak to a paraboloid and compute the peak shape, centroid, and amplitude for all frame pairs: discarding pairwise correlations between frames that show displacements greater than one or two pixels. More dramatic perturbations produce more severe distortions, so we discard for pairwise correlations that show correlation peaks with ellipticity or radii of gyration many standard deviations greater than the mean. This filtering process can be important for discriminating peaks in more mobile samples, where the peak correlation intensity may fall below the noise floor of our fitting algorithm. With emulsions, the large difference in thermal expansion coefficients between the glass tube and the oil droplets converts fluctuations in temperature into uniaxial strains. These strains can lead to irreversible rearrangements of the droplets and speckle intensity decorrelation; however, the air temperature in enclosure does not drift by more than $\pm 0.01°\text{C}$ during a typical measurement, so these strains are limited to amplitudes smaller than 10^{-4}.

Though it is not possible to simultaneously average many speckles with a single mode fiber optic detector, we manipulate the incident light to provide unbiased sampling. This can be done by placing a another multiply-scattering element between the sample and the detector, but this reduces the intensity and scrambles the polarization of the detected light. Instead we choose to deflect the incoming light using a large, transparent acrylic disc, as depicted in the schematic Fig. 3.1. The thickness of the

disk and its angle with the optical axis of the fiber determine the absolute deflection of the incident light. By rotating the disk at regular intervals we sample hundreds of independent speckles. As before, we place the fiber far enough away from the emulsion to sample only independent speckles, and deflect the light enough to randomize the intensity after every step. A larger angle of incidence will deflect the light more, but will also affect the polarization of the transmitted light more. This effect can be mitigated by placing a thicker disc at a shallower angle in front of the detector. We chose a disk 17 mm thick, with a normal pointed 10 degrees away from the optical axis of the fiber, and rotate it by 2.7 degrees every 90 seconds. This abrupt change between independent speckles produces an artificial decorrelation in the measured $g_2(\tau)$ which can be removed by dividing the measured correlation by $1 - \frac{\tau}{\mathrm{T}}$, where T is the period between steps.

3.4 Apparatus Stability and Calibration

We use a sintered pack of borosilicate beads and a block of polytetrafluoroethylene (PTFE, Teflon) to test the stability of our instrument. The speckle patterns of light scattered from these materials should be perfectly static; however, vibrations, temperature driven dilations of the sample, and drift of the lasing frequency will lead to changes in the interference pattern and thus decorrelation. The thermal expansion coefficient of the glass beads is negligible, but that of the Teflon block is comparable to that of our oil droplets. Consequently, by measuring the intensity autocorrelation of light backscattered from these two materials it should be possible to separate the effects of vibrations, laser fluctuations, and fluctuations in the temperature of the

sample. The intensity correlations measured for both materials are almost perfectly static. The intensity correlations measured for the Teflon block decay somewhat faster than those for the sintered beads, and mechanical vibrations introduce additional scatter in the data. Typical intensity autocorrelations measured for these reference samples are presented in Fig. 3.2.

The elastic moduli of these materials and the size of their scattering structures are too large for the amplitude of their thermally induced vibrations to exceed picometer scales. By contrast, the positions of micrometer scale droplets belonging to an emulsion with a shear modulus of a few Pa can be expected to fluctuate several nanometers. For diffusely backscattered light, the time dependence of the speckle intensities is related to these displacements by the following set of relations:

$$g_2(\tau) = \frac{\langle I(t+\tau)I(t)\rangle}{\langle I(t)\rangle^2} \tag{3.1a}$$

$$= \beta\, g_1(\tau)^2 + 1 \tag{3.1b}$$

$$\sqrt{\langle \Delta r(\tau)^2\rangle} = -\frac{\log(g_1(\tau))}{\gamma\, k} \tag{3.1c}$$

$$G = \frac{k_B T}{\pi R \,\langle \Delta r(\tau\to\infty)^2\rangle} \tag{3.1d}$$

The angled brackets in (3.1a) refer to averages over the CCD detector pixels or over the sequence of speckles sampled by the optical fiber. When the fluctuations in the electromagnetic field are gaussian, the Siegert relation (3.1b) can be used to recover the field-field correlation, g_1, from the measured intensity-intensity correlation, g_2. The parameter β is equal to 1 when a single component of the the intensity is sampled at a single point in space. The value of β decreases when: the area of the detector is comparable to the speckle size; more than one polarization mode is detected; the in-

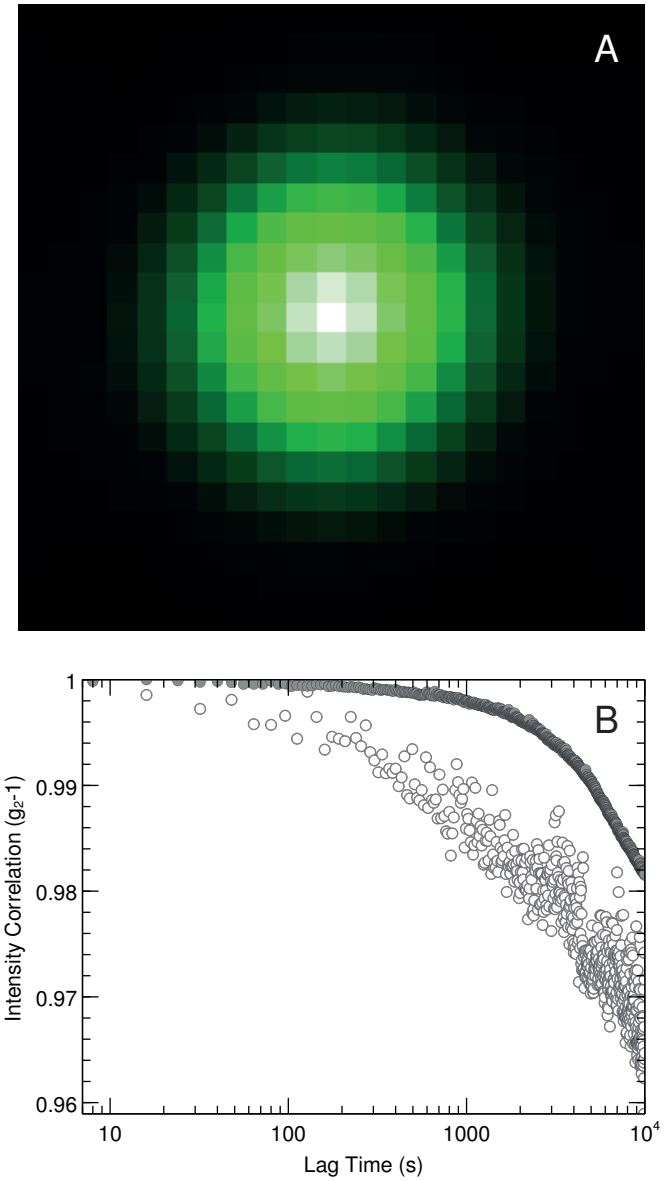

Figure 3.2: (A) Central portion of the spatial cross-correlation of laser light scattered from a sintered pack of borosilicate glass beads computed from frames gathered 8 s apart. (B) Intensity correlations for light scattered from a sintered glass bead pack (gray circles) and a Teflon block (open circles).

cident light has more than one statistically independent mode. The single mode fiber and polarizer effectively filter out all but a single statistically independent speckle, and β for this measurement is almost exactly equal to 1. However, the finite size of the CCD pixels lead to some spatial averaging that reduces the value of β to 0.8–0.9.

When the transport of light inside the opaque material can be assumed to be diffusive and absorption can be neglected, (3.1c) provides a direct relation between the speckle fluctuations and the mobility of the individual scatterers. Here, $k = \frac{2\pi\, n_{\text{eff}}}{\lambda}$ is the effective wavenumber of the laser light inside of the material, and γ is a parameter that typically lies between 1.5 and 2.5 and measures the typical length of the photon paths in units of l^*. This approximation assumes that the scattered correlation is dominated by contributions from long paths; however, the phase accumulated in longer paths decorrelates more quickly than that from shorter ones: (3.1c) is thus only valid when $-\log(g_1)$ is not much greater than 1. For $\lambda = 532\,\text{nm}$ and $\gamma \simeq 2$, this condition limits resolvable displacements to $\lesssim 50\,\text{nm}$.

The value of this RMSD is connected to the shear modulus of the emulsion by the GSER (3.1d). The frequency dependence of the viscoelastic shear modulus may be obtained from the analytic continuation of the Laplace transform of $\langle \Delta r(\tau)^2 \rangle$ along the imaginary frequency axis. This process requires that a suitable analytical model for $\langle \Delta r(\tau)^2 \rangle$ be fit to correlations spanning several decades in τ. However, for a material that behaves elastically at low frequencies, it is possible to extract the low frequency shear modulus by considering only the $\tau \to \infty$ limit of $\langle \Delta r(\tau)^2 \rangle$. To compute this limiting value from (3.1c) we must first determine the value of γ. It is possible to derive an analytical value for this parameter by assuming that

scatterers are spatially uncorrelated and that they perfectly randomize the direction of scattered photons. It is also possible to extract more realistic values of γ from photon path length distributions computed from elaborate simulations that account for the scattering anisotropy and the spatial correlation of scatterers. Instead, we fix γ by comparing DWS measurements to mechanical rheology. We cannot carry out these measurements on the sealed, sedimented sample, so we prepare a separate calibration sample with a bidisperse mixture of droplets and a shear modulus of $\simeq$10 Pa.

We first synthesize 3.6 μm and 4.5 μm polystyrene particles using seeded dispersion polymerization, clean them, and suspend them in a 3 mM solution of SDBS in water. We suspend approximately equal numbers of these particles in a 20 vol. % solution of D_2O with 3 mM SDBS, and add enough anisole to swell the particles to five times their original volume. After the anisole is absorbed by the particles, the emulsion is centrifuged at 15 g for several days while the clear subnatant is removed and stored. We measure the shear modulus of the concentrated emulsion using oscillatory shear in a double gap Couette geometry on a stress controlled rheometer (MCR501, Anton Paar), and replace enough of the stored subnatant to adjust the modulus to $\simeq$ 10 Pa. Swept frequency measurements show a nearly frequency independent storage modulus between 0.003 Hz and 0.05 Hz. Swept oscillatory strain measurements at 0.005 Hz show linear, elastic behavior for strains below 0.6 % (Fig. 3.3). The buoyant density of the swollen droplets in this suspension is $\simeq$ - 4 kg/m^3; therefore, the pressure difference between the top and bottom of the sample is $\lesssim$ 2 Pa.

We take 15 mL of this reference sample and seal it in a 4 cm wide, 1 cm deep, rectangular, glass cell. We place this sample in our temperature controlled enclo-

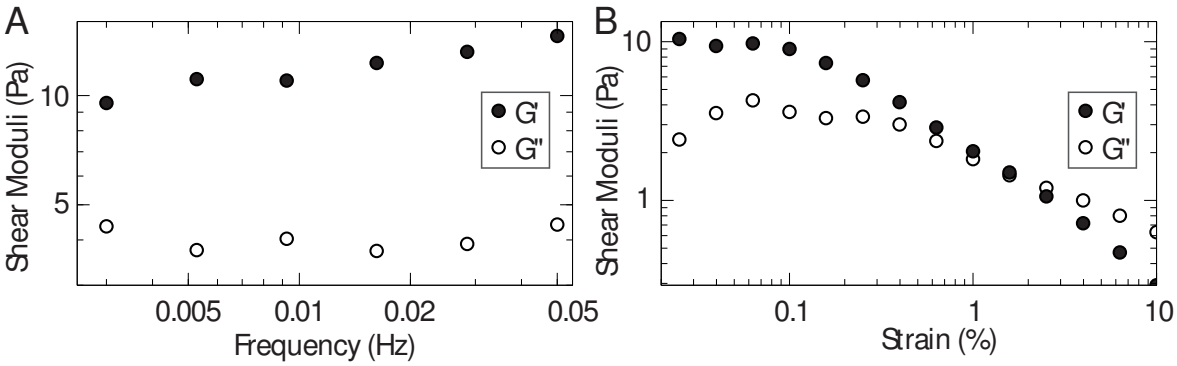

Figure 3.3: (A) Real and imaginary parts of the viscoelastic modulus of a compressed emulsion measured with oscillatory frequency sweeps with an oscillation amplitude of 0.05 %. (B) Real and imaginary parts of the response to 0.005 Hz frequency oscillatory strains with increasing amplitude.

sure, adjust the ambient temperature to 22°C, and wait one day before recording the scattered light intensity. To track the effects of sample aging we perform 20 hr long measurements on three consecutive days. Binning the intensity correlation data from these three measurements leads to the three correlation functions shown in Fig. 3.4A. All three measurements agree for lag times shorter than 100 s, but longer lag times clearly show the effects of effects aging. Measurements performed on aging samples are not stationary; the average described in (3.1a) should thus not be done over the waiting time, t, but over independent speckles. We compute a time resolved correlation (TRC) using the speckle images gathered with the CCD as:

$$g_2(\tau, t) = \frac{\langle I(t+\tau, x) I(t, x) \rangle_x}{\langle I(t+\tau, x) \rangle_x \langle I(t, x) \rangle_x} \tag{3.2}$$

Where x denotes the pixel coordinate. We thus plot the waiting time dependence of the intensity correlation for lag times of 1 000 s, 3 000 s, and 10 000 s in Fig. 3.4B. The correlation values for $\tau = 1\,000$ s, show some time dependence, but reach a fairly steady plateau, with scattered decorrelation avalanches, after 2 days of aging.

Correlation values for $\tau = 3\,000\,\mathrm{s}$ may have reached a plateau after 4 days, but have much larger decorrelation avalanches. By contrast, correlation values of $\tau = 10\,000\,\mathrm{s}$ show pronounced and persistent avalanches and may take many more days to reach a final plateau.

By contrast, the TRCs of emulsions that have aged for several months are almost perfectly stationary. Since it has been shown that, for moderately compressed emulsions, $\Pi \simeq G$, we compare this reference sample to one that has been aged for several months at an osmotic pressure of 9.5 Pa: equal to the value of the storage modulus measured at 0.003 Hz. At 31.5°C, the buoyant density of the sedimented droplets is $11\,\mathrm{kg/m^3}$; consequently, if we assume that the volume fraction of the column is $\simeq 0.65$, a pressure of 9.5 Pa is equivalent to a depth below the top of the sediment of 14 cm. We plot the intensity correlation (Fig. 3.4A, black) and the corresponding TRCs (Fig. 3.4C) gathered at this depth after many months of aging at constant temperature. Since we cannot access oscillatory frequencies comparable to 1/10 000 Hz or aging times of several weeks on the rheometer, it seems appropriate to compare these samples at for lag times $\lesssim 1\,000\,\mathrm{s}$. The measured intensity correlations for the aged and reference samples clearly agree for short and intermediate lag times: though they deviate at lag times were the effects of aging in the reference are readily apparent. Despite a fair amount of variability, the TRCs measured for the aged sample appear stationary, even for very long lag times.

Thermal fluctuations cause not only fluctuations of the droplet center positions, but also the fluctuation of the droplet interfaces. The amplitude of these thermocapillary waves is $\sim \sqrt{\frac{k_B T}{\sigma}} \simeq 1\,\mathrm{nm}$, where σ is the interfacial tension of the droplets. Since

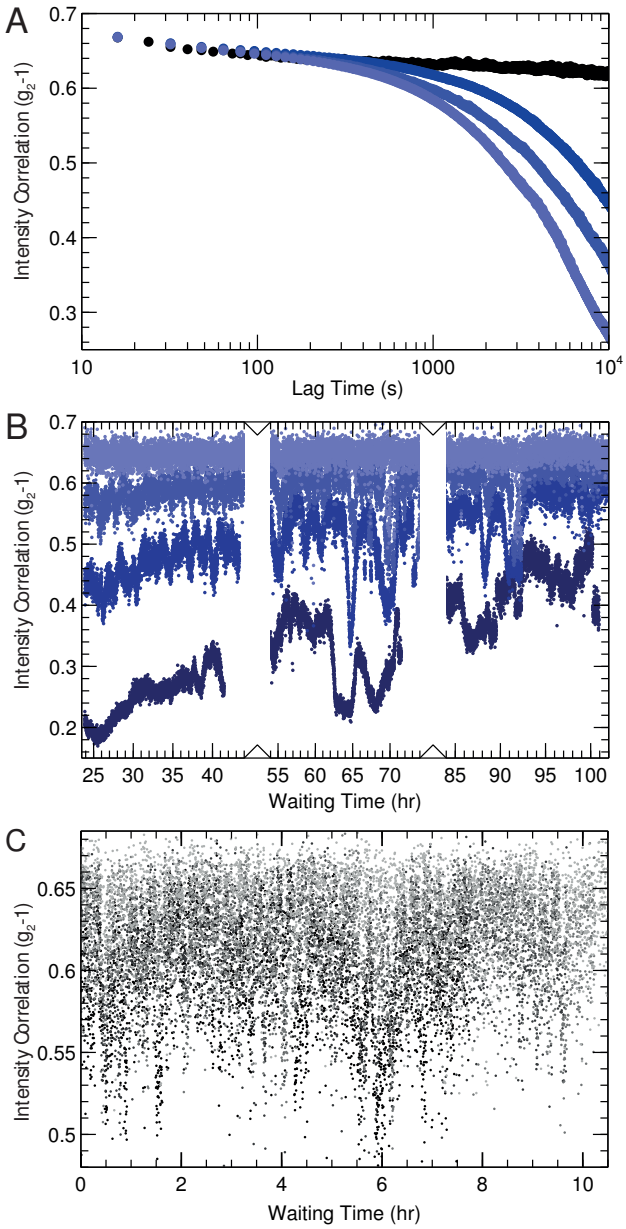

Figure 3.4: (A) Binned intensity correlations for samples aged for one, two, and three days (light to dark blue), as well as a sample aged for several months. (B) Time resolved correlations (TRC) for the aging sample measured at lag times of 100 s, 1 000 s, 3 000 s, and 10 000 s (light to dark blue). (C) Time resolved correlations (TRC) for the equilibrated sample measured at lag times of 100 s, 1 000 s, 3 000 s, and 10 000 s (gray to black).

positional fluctuations are not strongly correlated to the interfacial fluctuations, these two fluctuations contribute additively to $\langle \Delta r(\tau)^2 \rangle = \langle \Delta r(\tau)^2 \rangle_{pos} + \langle \Delta r(\tau)^2 \rangle_{int}$, whith $\frac{\langle \Delta r(\tau)^2 \rangle_{int}}{\langle \Delta r(\tau)^2 \rangle_{pos}} \ll 1$. Moreover, the lifetime of these interfacial fluctuations, $\tau \sim \frac{R\eta}{\sigma} \simeq 5\,\mu$s, is too short to be resolved by our camera with our $63\,\mu$s exposure time. The measured pixel intensities thus average over many configurations of the interfacial fluctuations, and these displacements are absorbed into an effective β that is reduced, from 0.8–0.9 in the case of sintered beads, to $\simeq 0.7$ for our emulsions. By dividing the measured intensity correlations by this effective β we effectively eliminate the contribution of interfacial fluctuations from our measurement of $\langle \Delta r(\tau)^2 \rangle$.

If we replace the $\tau \to \infty$ limit in (3.1d) with $\tau = 10\,000$, and use (3.1a-c) to compute $\langle \Delta r(\tau = 10\,000)^2 \rangle$, we can equate the the shear modulus of the reference sample with that of the aged sample by choosing $\gamma = 2.27$. This value of γ is within the commonly observed range for this parameter, but choose to set $\gamma \equiv 2$ to compute the shear moduli of the quiescent emulsion. The difference between shear moduli computed with either value of γ is less than 30%, and simply rescales $G(\Pi)$ by a constant factor.

Chapter 4

Compressibility of Jammed Emulsions

A dilute dispersion of fluid droplets behaves as viscous liquid, but a concentrated emulsion is an amorphous, solid-like material. For purely repulsive, surfactant stabilized droplets, the transition between these two states occurs at a precise droplet volume fraction, ϕ_c. The deformability of the droplet interfaces makes it possible to increase the packing density even further, and the elastic properties of the solid depend on this excess volume fraction, $\delta\phi = \phi - \phi_c$. Close to this liquid-to-solid transition, small changes in ϕ lead to large changes in elasticity, and preparing bulk samples with precise enough control over their composition is extraordinarily difficult. By contrast, the osmotic pressure, Π, just above this critical volume fraction is small, and small variations in the applied pressure lead to small variations in the elastic constants. However, controlling Π below $\sim 10\,\mathrm{Pa}$ is also challenging and the solid, though elastic, is too soft and weak to be probed mechanically. Consequently,

non-invasive methods to control Π and measure the elasticity of the emulsion are necessary.

We have shown that it is possible to measure the shear modulus, G, of a quiescent pile of droplets close to this jamming threshold using non-invasive light scattering. Instead of controlling the volume fraction, we set the osmotic pressure of the emulsion using the gravitational stress of the droplet pile. When the pile reaches mechanical equilibrium, the pressure at a depth, d, into the sediment is set by the integrated stress:

$$\Pi(d) = g\,\delta\rho \int_0^d \phi(z)\,\mathrm{d}z$$

The smallness of $\frac{\delta\phi}{\phi_c}$ allows us to ignore the variations in droplet volume fraction when determining $G(\Pi)$. Nevertheless, the variation of the pressure along the depth of the pile naturally sets $\phi(\Pi)$, and the high resolution required to measure this quantity requires a new, non-invasive technique.

Here we show that it is possible to measure $\phi(\Pi)$ with a volume fraction resolution below 0.1% using a high resolution nuclear magnetic resonance (NMR) spectrometer (DD2 600, Agilent and 14.1 T superconducting magnet) equipped with a pulsed field gradient probe (5 mm indirect detection with PFG, Agilent). We make droplets of silicone oil (PDMS) and tetrachloroethylene (TCE) in D_2O and develop radio frequency (rf) pulse sequences to image both the proton and deuterium signals present in these samples. We design thoroughly compensated, spin and gradient echo sequence to measure the variations in proton signal intensity with high spatial and mass resolution, and use a measurement of the depth dependence of the deuterium signal to convert this relative intensity signal into a quantitative volume fraction measurement.

4.1 Design of Imaging Pulse Sequence

Magnetic imaging or sectioning techniques can be divided into three broad categories: selective excitation, phase encoding, and read gradients [15]. All three modalities rely on pulsed magnetic field gradients that temporarily shift the resonant frequency of the measured spins based on their position. A selective excitation sequence applies frequency selective pulses while the gradient coil is energized (Fig. 4.1a). Though the assumption that these coils apply a perfectly uniform gradient along the direction of the principal field is unphysical, a frequency selective pulse can be designed to excite nuclear spins within a specific slab of material. The precession of the spins in the field induces a current in the coil that can then be translated into the mass contained in the excited volume [15]. The spatial resolution of this method is limited by the strength of the applied gradient and the bandwidth of the excitation pulse: which is inversely proportional to the pulse length.

Phase encoding techniques use broadband pulses to excite all of the material, and energize the gradient coil for some prescribed time before the induced current is measured (Fig. 4.1b). Within the approximations of the Bloch-Torrey equations [86], the phase of spins precessing in a constant magnetic field with an additional gradient, $\vec{B} = B_0\hat{z} + G\,(-x\hat{x}/2 - y\hat{y}/2 - z\hat{z})$, will depend on their position in space:

$$\psi(\vec{r}, t) = t\,(\omega_o + \gamma_o\, G\, z)$$

where γ_o is the gyromagnetic ratio of the measured nucleus, and ω_o is the difference between the natural precession frequency of the spin and that of the rotating reference frame. Measurements of the amplitude and phase of the nuclear magnetization

as a function of gradient amplitude or encoding time are thus equivalent to measurements of the Fourier transform of the mass density. If time evolution of each of the acquired signals is further decomposed into independent frequency components, this measurement can be used to resolve the spatial and chemical composition of the material [15]. However, reconstructing density profiles with high resolution requires a very large number of measurements.

Gradient echoes are the simplest of these measurement techniques. Here, all the spins in the measurement volume are excited using a broadband pulse, the gradient is then turned on for some time, and subsequently reversed (Fig. 4.1C). If the amplitude and phase of the magnetization is gathered for the entire duration of the second gradient pulse, its Fourier transform corresponds to the density profile. This technique assumes that each frequency component of the spectrum corresponds to a separate spatial positions; however, when two or more chemically distinct nuclei are present, the resulting spectrum is a convolution of the spatial distribution of spins with their chemical frequency spectrum: this is know as a chemical shift artifact [15]. High resolution NMR spectrometers used for chemical analysis are capable of recording these signals with extremely high accuracy and temporal resolution, so this modality is the best suited for the kind of tomographic measurement we would like to perform.

The simple rf and field gradient pulse sequences described in Fig. 4.1 are adequate for measurements where qualitatively correct densities are sufficient. To improve the accuracy of the measurement of proton densities we use the pulse sequence depicted in Fig. 4.2A. To the simple bipolar gradient echo we add a two composite spin refocusing pulses. These refocusing pulses minimize the loss of signal that arises from the

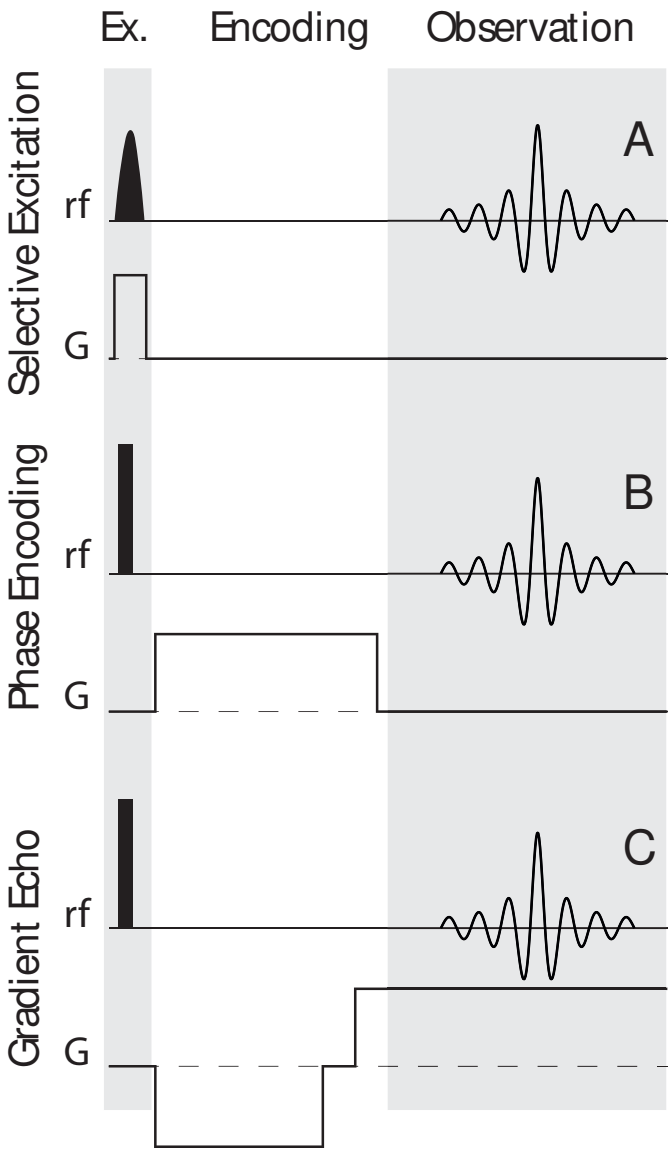

Figure 4.1: Simplest implementation of magnetic imaging sequences. (A) Selective excitation sequences excite the spins while the gradient coil is energized. (B) Phase encoding sequence use the spatial variations in the accumulated phase when spins precess in an inhomogeneous field. (C) Gradient echos use a gradient to dephase the spins in a sample, then reverse it to produce a burst of magnetization.

natural dephasing of the precessing nuclei. This dephasing comes from the natural precession lifetime, T_2, of nuclei and from the slight inhomogeneities in the magnetic field caused by the difference in the magnetic susceptibilities of the oil and water. We chose a composite 90_α-90_β excitation pulse to collect as much signal as possible and choose paired, composite, 90_δ-180_γ-90_δ refocusing pulses to compensate for the non-uniformity of the rf field generated by the probe coil. The refocusing pulses must be matched to avoid introducing phase offsets [40, 54, 55]. We account for the finite time of the excitation pulse by shortening the time before the first refocusing pulse by $\frac{2\,\tau_{90}}{\pi}$, where τ_{90} is the duration of a single excitation pulse [39]. We compensate for imperfections in the shape of field gradient pulses by adjusting the start of the read gradient such that the echo is centered. This double spin echo sequence also allows us to use bipolar field gradient pulses, which minimize the effect of field gradients induced by eddy currents, and place the first gradient pulse immediately after the composite excitation pulse to minimize the effects of radiation damping [46]. This last artifact is due to the high concentration of spins in the measurement volume coupled to a probe coil with a high resonant quality factor (Q). When all the spins are excited at once, the precessing spins induce a current in the rf coil that then produces an oscillating magnetic field that interacts with the spins. When the proton density or the quality factor of the coil are low, this second order effect is negligible: neither condition is true of this measurement. By applying a large gradient immediately after the spins are excited we spread out their resonant frequency, which quickly leads to destructive interference that is not reversed until the read gradient refocuses the signal. The full phase cycling table is reported in Table 4.1.

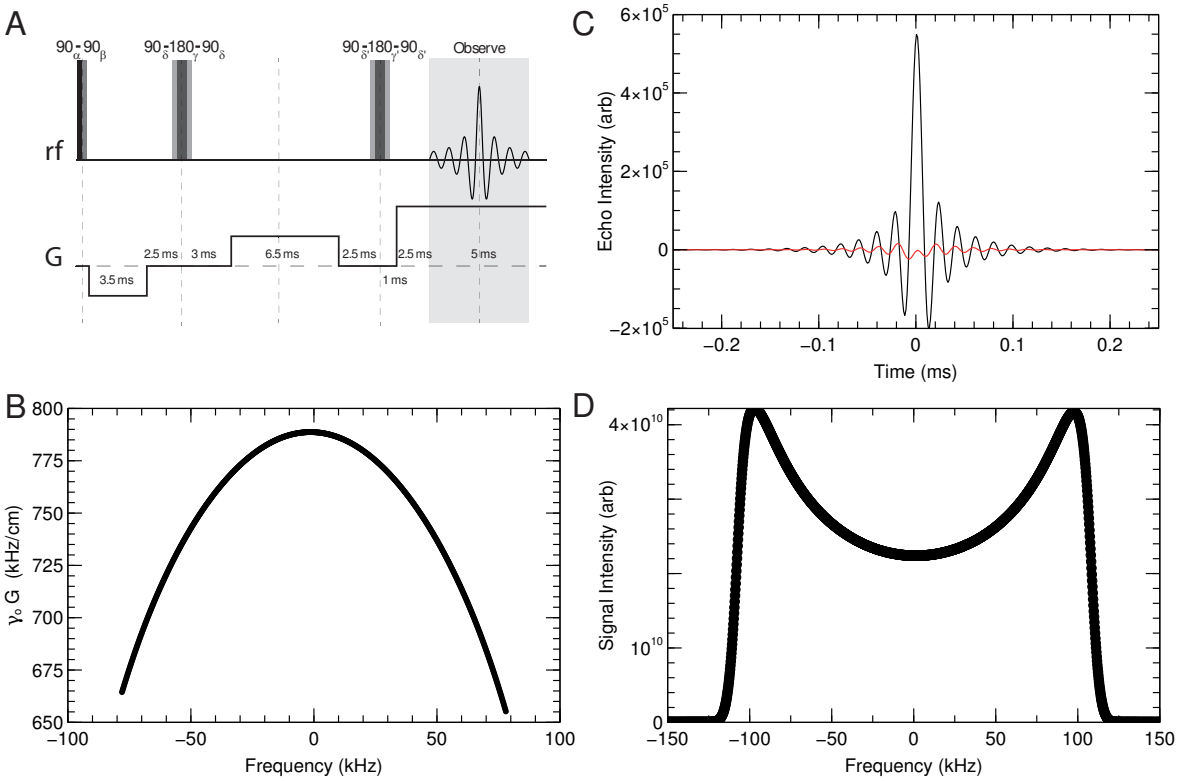

Figure 4.2: (A) Gradient echo sequence for proton densitometry. Double spin-echo with composite excitation and inversion pulses corrects for static field gradients and probe power deficiencies. (B) Magnitude of field gradient applied by PFG coil measured by diffusion attenuation. (C) Real (black) and imaginary (red) components of the echo signal produced by a uniform D_2O/H_2O sample. (D) Absolute value of the Fourier transform of echo in (C).

4.2 Calibration and Data Analysis

We test this sequence with 5 mm NMR tube (542-PP-7, Wilmad-LabGlass) filled with a 40:60 weight ratio mix of H_2O (Millipore) and D_2O (99.9 % DLM-4, Cambridge Isotope). We load the tube in the magnet, set the temperature of the forced air supply to 23°C, and wait for thermal gradients to dissipate. We use an inversion recovery pulse sequence, a population inverting 180° pulse followed by a variable waiting period and a 90° excitation pulse, to measure the longitudinal relaxation time of the spins, $T_1 \simeq 4$ s. This relaxation time sets the rate at which the memory of past measurements is erased, and so we choose to wait 20 s between measurements for the magnetization of the spins to return to equilibrium. We present a representative echo gathered using this sequence and the absolute value of its Fourier transform in Fig. 4.2C-D.

If the magnetic field gradient and the signal intensity generated by the rf coil were perfectly uniform, it would be possible to directly convert the Fourier transform of the signal intensity, $|I(\omega)|$, into a measurement of the density profile, $\rho(z)$; however, the rf and gradient coils and not infinitely long and have subtle imperfections that affect the measured signal intensity. For materials with small magnetic susceptibilities, the variations in the field gradient and detector response can be measured on a reference sample and removed.

Magnetic field gradient calibration

The magnetic field experienced by nuclear spins attached to diffusing molecules will vary depending on their position. Consequently, the accumulated phase will

depend on the molecule's trajectory:

$$\psi(\vec{r},t) = \gamma_o \int_0^T (B(z(t),t) - B_o)\,\mathrm{d}t$$

and perfect refocusing is not generally possible. When averaged over a macroscopic number of spins that follow unbiased random walks, this dephasing becomes an incoherent attenuation of the raw signal [72, 73]. For unconstrained diffusion, the attenuation of the signal can be expressed as:

$$\log \frac{I(G(\omega))}{I(G(\omega)=0)} = -A\,D\,\gamma_o^2\,G(\omega)^2$$

where D is the diffusion constant of the molecules, and A is a constant determined by the timing of the pulse sequence. The diffusion constants for H_2O/D_2O water mixtures is know [35], and A can be computed easily. Thus, we compute $\frac{\mathrm{d}\omega}{\mathrm{d}z} = \gamma_o\,G(\omega)$, and recover $z(\omega)$, from the signal attenuation measured at every frequency. The gradient intensity profile measured using our H_2O/D_2O reference is shown in Fig. 4.2B.

rf signal intensity calibration

rf coils for high resolution NMR are designed to have a nearly binary induced field profile. The resonant rf field rotates the magnetization about an axis normal to $B_0\hat{z}$, by an angle that is proportional to the rf pulse duration and field intensity. A uniform field near the center of the coil produces a large population of evenly excited spins; a rapid decay of the intensity towards the edges of the coil minimizes the number of spins that receive less than a full dose of the intended rf pulse. The same coil that produces these rf pulses is also used to measure the current induced by the precessing magnetization; the excitation and collection efficiencies are, therefore, equal. These

variations in the spatial response of the probe are reflected in the rapid decay of the signal measured at higher frequencies (Fig. 4.2D). To minimize the error due to miscalibrated pulse power, we choose to keep data from regions of the spectrum that are far enough from the edges of the coil. We also compensate for smaller variations in the uniformity of the rf field intensity with composite excitation and inversion pulses [40, 54, 55]. Despite these corrections, it is still not possible to find a single rf pulse duration that maximizes the measured signal intensity in the entire middle portion of the coil.

The rf field induced by the coil in our spectrometer is slightly larger near the top of the sample than the bottom. The duration of the pulse that optimizes the signal collected from the top of our active region is close to 8% shorter than that which maximizes the signal from the bottom. Though our sequence reduces the difference between the optimal and median signal intensity to $\lesssim 1\%$, such a systematic error is not acceptable for high resolution densitometry. We address this shortcoming by recording echos using pulse lengths that bracket the median pulse duration by at least $\pm 5\%$. We then fit a polynomial to the intensity measured at every frequency, and find the optimal pulse duration for each frequency, $\tau(\omega)$, and the optimal signal intensity, $I^*(\omega)$. For samples with proton concentrations of at least 10 M we find that the reproducibility of this measurement is $\simeq \pm 0.03\%$.

Diffusion attenuation calibration

The free diffusion of molecules in a field gradient provides a convenient way to calibrate the field profile and generates a uniform attenuation that can be divided

out and ignored in uniform samples. However, the diffusion of molecules contained inside of droplets or in the space between droplets is hindered by these impenetrable interfaces [15, 83, 95–97] Moreover, small differences in the magnetic susceptibilities of the materials in the imaging volume produce static magnetic field gradients that also contribute to the attenuation of the signal. The attenuation of the magnetic signal in non-uniform materials thus depends on the local structure of the medium in a way that is not trivial.

When the static field gradients induced by the contrast in magnetic susceptibilities is small, their contribution to the signal attenuation can be nearly eliminated using the 180° refocusing pulses included in our sequence; the remaining signal attenuation then depends on $|G^2|$. We record echos at several values of G and compute the $G \to 0$ limit of $I^*(\omega)$. The resulting signal is reproducible and well defined, but is still affected by the shape of the spatial response function of the rf coil, and possible variations in the shape of the tubes that hold the sample. Yet, these contributions do not depend on the material contained in the tube, so we generate a reference for each tube by performing the full set of measurements required to obtain $I^*(\omega, G \to 0)$ on uniform fluid samples. When the pulse sequence duration is much shorted than the transverse decorrelation time of the magnetization, T_2^*, and the time between measurements is much longer that the longitudinal relaxation time, T_1, the density profile is recovered by dividing the measured $I^*(\omega, G \to 0)$ by the stored reference.

4.3 Preparation of Monodisperse Emulsion Sediment

Our gradient echo sequence works best when measuring chemically identical nuclei; we thus use 20 cSt PDMS as the source of proton signal, and D_2O as the source of deuterium. The natural abundance of deuterium is low enough that we need not worry about deuterium signal arising from the PDMS, and the content of hydrogen in high purity D_2O is also negligible. The final concentration of SDBS is also small enough to be negligible. We begin by emulsifying PDMS using a cylindrical, porous glass membrane (Shirasu Porous Glass, 1 cm outer diameter, 2 cm long, 3 μm pore size). We clean the membrane by soaking it in a potassium hydroxide solution and rinse it with deionized water. We then mount it on a stainless steel holder equipped with two o-rings and a fluid inlet. To avoid trapping air in the membrane we flow CO_2 through the pores and submerge the assembly into a solution of 10 mM sodium dodecyl sulfate (SDS). After the chamber is purged, we shut off the flow of gas and use a vacuum to draw the SDS solution into the membrane assembly. We then connect the assembly to a syringe filled with the PDMS using a three way valve, and use a syringe pump to push oil through the membrane at a constant rate [16, 91]. Droplets formed using such a device can be polydisperse; however, when we operate the device at 1 ml/hr we obtain droplets with a mean diameter of 10 μm and a standard deviation of 0.8 μm.

We increase the density of the droplets by swelling them with an equal volume of tetrachloroethylene, dividing the addition into three steps. We first add one third the

necessary TCE to the suspension of droplets and tumble them until the oil has been absorbed. These droplets are denser than D_2O, but not heavy enough to coalesce while still dispersed in water. We allow the droplets to settle and replace the supernatant with a 3 mM solution of SDBS in D_2O and add half of the remaining TCE. The emulsion is tumbled until the TCE is absorbed, and the process is repeated for the last aliquot of TCE. To remove the residual SDS and water from the initial emulsification we allow the droplets to settle and replace the supernatant with a 2 mM solution of SDBS in TCE saturated D_2O. Though this process removes most of the SDS, dodecanol impurities found in the SDS solution cannot be removed and lower the interfacial tension of the droplets.

4.4 Proton Imaging

We load a 45 vol. % solution of tetraglyme in D_2O into a 5 mm NMR tube and collect a reference measurement of the coil response and tube shape. We clean the tube by rinsing it several times with a 2 mM solution of SDBS in D_2O and add enough of a 20 vol. % dispersion of these droplets to it for the resulting sediment to nearly fill the imaging volume. The droplets are allowed to settle while the tube is held vertically. After the sediment is formed we add more of the SDBS solution to the tube and seal it with fluorinated grease (Krytox LVP, Dupont) and a Teflon cap (WG-1264-5, Wilmad-LabGlass). We anneal the sediment by storing the tube alternatively at 20°C and 27°C, changing the temperature eight times over two days. The temperature cycling causes droplet volumes to fluctuate by $\sim$1%, but the volume of the borosilicate glass tube remains almost constant. This mismatch converts the

changes in droplet volume into uniaxial strains.

After waiting one week for the sample to equilibrate at room temperature we load it into the spectrometer and set the temperature control to 23°C. While we wait for the temperature of the sample to equilibrate we measure the transverse and longitudinal relaxation times, and shim the magnetic field. The longitudinal relaxation time, $T_1 \simeq 1.7\,\mathrm{s}$, so we set the time between measurements to 12 s. We monitor the position of the interface while all the necessary combinations of rf pulse length and field gradient strength are executed. This procedure lasts about five hours, and we use the shape of sequential echos to confirm that the interface does not move appreciably during this time.

When the reference sample is not composed of the material that composes the sample we want to image, the measured signal is proportional to the mass density, but is not equal to it. We chose to use a D_2O/tetraglyme solution with a similar proton concentration as a reference for this sample; however, without a reference that matches the signal of the pure PDMS/TCE mixture exactly, we cannot produce quantitative volume fraction measurements. Instead, we image the deuterium in the surrounding fluid and use this as an absolute, internal reference of the volume fraction.

4.5 Internal Deuterium Reference

The deuterium nucleus has a spin of 1, and the three level angular momentum states are coupled by the electric dipole moment of the nucleus. This coupling can make deuterium spectroscopy more complicated than proton spectroscopy, but, for nuclei that are free to rotate quickly, this coupling only results in faster relaxation

rates. The resonant frequency of deuterium is also much smaller than that of hydrogen. This reduces the signal intensity and extends the precession times by an order of magnitude [14, 15, 26, 34]. To compensate for these effects we use larger gradient strengths, and shorter, simpler pulse sequences (Fig. 4.3A and Table 4.2). This makes it difficult to obtain high resolution density profiles from deuterium imaging alone. Nevertheless, we can use the ratio of the deuterium signal just above the top of the sedimented emulsion to that just below it as an internal reference for ϕ^*, the critical volume fraction. We still need to compute the $G \to 0$ limit of the signal intensity to measure this number; yet, because the measurement only needs to be accurate in a small neighborhood of the top of the sediment, careful pulse timing calibrations are not necessary. A representative echo signal is shown in Fig. 4.3C.

The sharp interface between the emulsion and supernatant causes ringing in the echo signal, and, since the precession frequency is much smaller than that of hydrogen, the measurement time required to fully capture this slowly decaying oscillation becomes comparable to the transverse decorrelation time of the precessing magnetization. However, because the ringing is caused by a discontinuous density profile, we can fit this oscillation to one produced by a model step discontinuity and subtract it from the echo. We choose a step with the form:

$$\hat{\rho}(\omega) = H(\omega - \omega_0)\, e^{-(\omega-\omega_0)^2/a^2} e^{i(\theta_0+\theta_1\cdot(\omega-\omega_0))}\, b\,(1 + c\cdot(\omega-\omega_0))$$

where $H(\cdot)$ is the Heaviside step function, ω_0 is the position of the interface, θ_0 and θ_1 adjust the phase and timing of the echo, b sets the magnitude of the jump in the density, c corrects for higher order oscillations due to discontinuities in the slope of the signal across the discontinuity, and a sets the width of the Gaussian cut-off. The

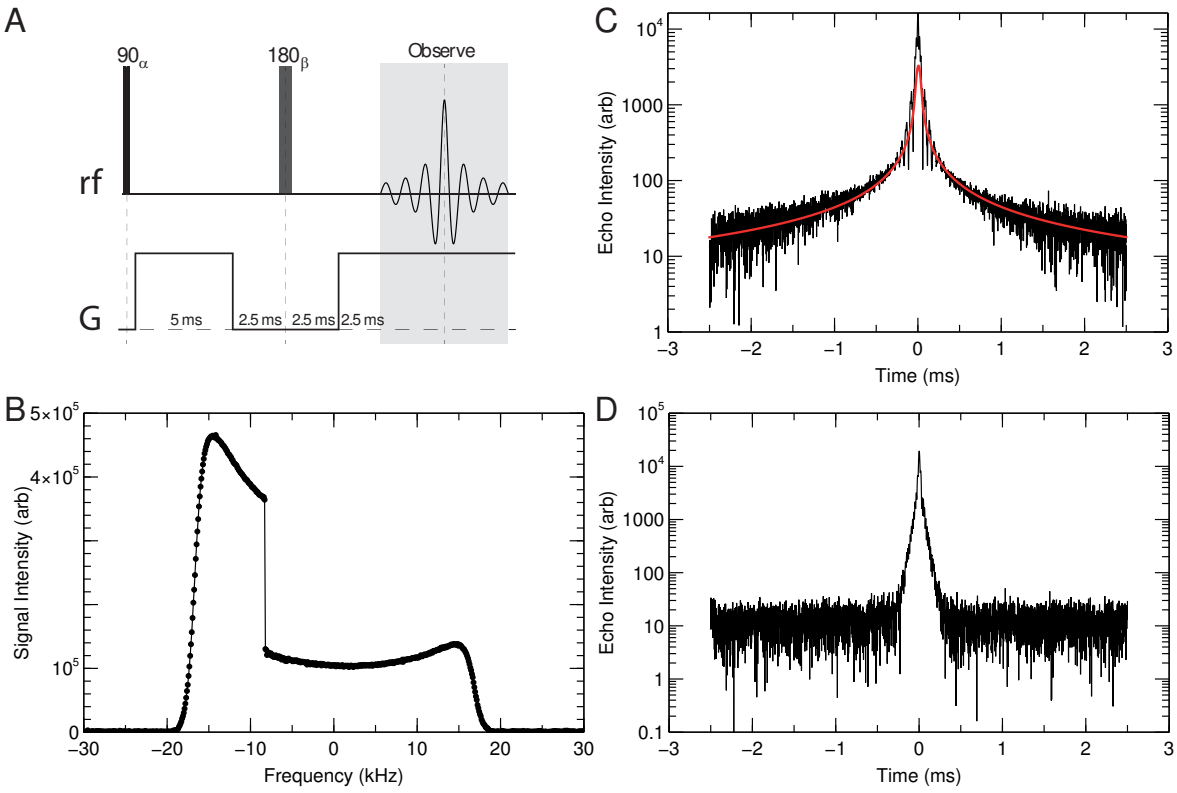

Figure 4.3: (A) Gradient echo sequence for deuterium densitometry. Single spin-echo reduces the effects of static field gradients. (B) Fourier transform of the extended echo signal produced by adding and subtracting a step-Gaussian density from the measured echo. (C) Absolute value of the measured echo (black) and step-Gaussian fit (red) for deuterium imaging of sedimented droplets. (D) Absolute value of the difference between the measured echo and the step-Gaussian function.

Fourier transform of this discontinuous function precisely captures the shape of the oscillations, and the difference between the measured echo the model echo decays below the noise floor well within the measurement window (Fig. 4.3D). To recover the correct shape of the raw density profile we add $\hat{\rho}(\omega)$ back to the Fourier transform of the subtracted echo (Fig. 4.3B). After repeating this process for several values of G, we recover the absolute value of the droplet volume fraction at the top of the sediment from the $G \to 0$ limit of $\phi_c \equiv 1 - \frac{I^*(\omega \to \omega_0{}^+)}{I^*(\omega \to \omega_0{}^-)}$. We use this value to normalize

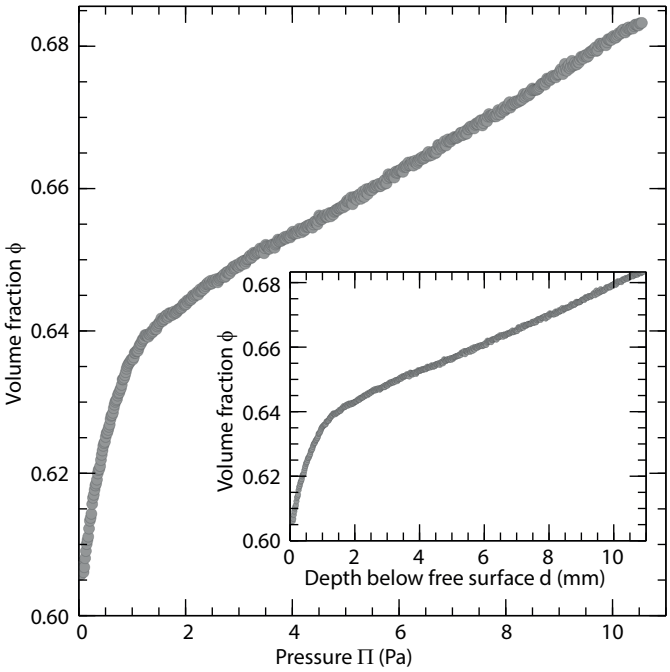

Figure 4.4: Droplet volume fraction as a function of sediment pressure and depth (inset). Data from high resolution proton densitometry is scaled by the internal density reference derived from lower resolution deuterium densitometry.

the density profile presented in Fig. 4.4.

	Rotation Axis					
Cycle	α	β	γ	δ	γ'	δ'
1	y	x	x	y	x	y
2	y	-x	x	y	x	y
3	y	x	-x	-y	x	y
4	y	-x	-x	-y	x	y
5	y	x	x	y	-x	-y
6	y	-x	x	y	-x	-y
7	y	x	-x	-y	-x	-y
8	y	-x	-x	-y	-x	-y
9	y	x	-y	x	-y	x
10	y	-x	-y	x	-y	x
11	y	x	y	-x	-y	x
12	y	-x	y	-x	-y	x
13	y	x	-y	x	y	-x
14	y	-x	-y	x	y	-x
15	y	x	y	-x	y	-x
16	y	-x	y	-x	y	-x
17	y	x	x	-y	x	-y
18	y	-x	x	-y	x	-y
19	y	x	-x	y	x	-y
20	y	-x	-x	y	x	-y
21	y	x	x	-y	-x	y
22	y	-x	x	-y	-x	y
23	y	x	-x	y	-x	y
24	y	-x	-x	y	-x	y
25	y	x	-y	-x	-y	-x
26	y	-x	-y	-x	-y	-x
27	y	x	y	x	-y	-x
28	y	-x	y	x	-y	-x
29	y	x	-y	-x	y	x
30	y	-x	-y	-x	y	x
31	y	x	y	x	y	x
32	y	-x	y	x	y	x

Table 4.1: Partial phase cycling table for the compensated, proton imaging pulse sequence. Phases of the rotation pulses are specified by the axis about which they rotate the magnetization. Full phase cycling table includes the reflected sequence ($\alpha \to -\alpha$, $\beta \to -\beta$, $\gamma \to -\gamma$, etc.).

	Rotation Axis	
Cycle	α	β
1	y	y
2	y	-y
3	y	x
4	y	-x
5	-y	-y
6	-y	y
7	-y	-x
8	-y	x
9	-x	-x
10	-x	x
11	-x	y
12	-x	-y
13	x	x
14	x	-x
15	x	-y
16	x	y

Table 4.2: Complete phase cycling table for the deuterium imaging pulse sequence. Phases of the rotation pulses are specified by the axis about which they rotate the magnetization.

Chapter 5

Elasticity of Pickering emulsions

A dispersion of liquid droplets in a fluid behaves like a solid when droplet interfaces are forced to touch. The fluids themselves bare no stress, and the droplet interfaces are thermodynamically unstable, but an adsorbed monolayer of surfactant molecules or solid particles can prevent droplet interfaces from coalescing and determines how these interfaces interact with each other. When droplets are covered with surfactant molecules that provide short-ranged and repulsive droplet interactions, the elasticity of their emulsions is universal: solid-like behavior emerges at a critical volume fraction, ϕ_c, above which droplets are forced to press against each other; the elastic moduli are proportional to the ratio of the interfacial tension to the typical droplet radius, $\frac{\sigma}{R}$; above ϕ_c the osmotic bulk modulus, K, is nearly constant and the shear modulus, G, increases like $\frac{\sigma}{R}\,\phi\,(\phi - \phi_c)$ [60, 62, 74, 75].

The mechanical properties of Pickering emulsions, emulsions stabilized by solid particles [71, 77], are remarkably similar to those stabilized by surfactants: despite the vastly different mechanical properties of particle and surfactant stabilized fluid

interfaces. The adsorption free energy of solid particles at fluid interfaces can easily exceed hundreds of k_BT, and interfaces that are densely packed with such strongly bound particles behave like elastic solids that buckle and yield [29, 84, 87]. Since the elasticity of these interfaces is determined by the size of the bound particles, this dimension could affect how the elastic moduli of the emulsions scale with droplet size; however, the shear modulus of compressed, Pickering emulsions increases like $\frac{\tilde{\sigma}}{R}\,\phi\,(\phi - \phi_c)$ [2, 50]. This scaling function is identical to that of surfactant-stabilized emulsions, however, the apparent interfacial tension, $\tilde{\sigma}$, is typically an order of magnitude larger than the equilibrium tension, σ, and does not seem to depend on the size of the adsorbed particles. It is not clear how adsorbed solids can give rise to such large apparent interfacial tensions, or why the value of $\tilde{\sigma}/\sigma$ produced by adsorbed proteins is comparable to that produced by adsorbed microparticles [2, 11, 50], but for $\tilde{\sigma}$ to act as a true interfacial tension it must affect the elastic moduli and strength equally. However, droplet flocculation and gelation interferes with measurements of emulsion compressibility and yielding, and obscures the intrinsic properties of solid-stabilized droplet mechanics.

Here we show that the adsorption of solid particles to fluid interfaces dramatically increases the shear stiffness but does not affect the osmotic compressibility or the shear strength of solid-stabilized emulsions. We study emulsions composed of repulsive, nanoparticle-stabilized droplets. Monolayers of strongly bound particles are formed on droplet interfaces by agitation, and the emulsification process follows the limited coalescence mechanism. When the volume fraction of these emulsions exceeds $\phi_c \gtrsim 0.6$ their shear modulus scales like $\frac{\tilde{\sigma}}{R}\,\phi\,(\phi - \phi_c)$, and is otherwise zero. Though the

dependence of the shear modulus of these Pickering emulsions on volume fraction and droplet size is the same as that of surfactant-stabilized emulsions, their stiffness is an order of magnitude greater; nevertheless, we find that the shear strength and osmotic compressibility of these particle-stabilized emulsions are equivalent to those of surfactant-stabilized emulsions. Consequently, the addition of particles to the interface does not simply increase its interfacial stress, $\tilde{\sigma}$.

The binding energy of such solid particles is determined by the particle size, interfacial tension, and liquid-liquid-solid contact angle that these particles adopt at the interface. We choose sterically stabilized silica nanoparticles (Tol-ST, Lot 190959, 10–15 nm diameter, Nissan Chemical) dispersed in toluene or chlorobenzene as our solid stabilizer. These particles form stable dispersions in these liquids and stabilize droplets of water and other polar liquids in these oils. Ethylene glycol and chlorobenzene are nearly isopycnic, and emulsions of ethylene glycol in chlorobenzene are ideally suited for rheological measurements. By contrast, the density of ethylene glycol is substantially larger than that of toluene: we use emulsions of these two fluids to study the elasticity of emulsions under gravitational stress. We measure the interfacial tension of these two oils with ethylene glycol using pendant drop and DuNouy ring tensiometry (Sigma 700, KSV) [37, 38], and find $\sigma \simeq 7\,\mathrm{mN/m}$ for chlorobenzene and $\sigma \simeq 9\,\mathrm{mN/m}$ for toluene. This tension is lower than that of water-oil systems, and the small particle diameter limits the binding energy to $\leq 200\,k_BT$, but this barrier is large enough to prevent spontaneous desorption. Though not absolutely irreversible, the binding energy of the particles to these interfaces is strong enough to force the emulsification process to follow the limited coalescence mechanism.

Unlike surfactant molecules that quickly equilibrate between micelles and droplet interfaces, the total mass of irreversibly bound particles, M, determines the maximal interfacial area that can be densely covered with them. This fixed area, together with a fixed dispersed phase volume, V, defines a typical droplet diameter, $\bar{R}$, that scales like V/M. The fluid interfaces of an emulsion composed of droplets much smaller than $\bar{R}$ cannot be densely covered with particles, and are prone to coalescing until the all the excess interfacial area is destroyed. Therefore, when the unbinding rate of particles is negligible compared to the rates of droplet breakup and coalescence, the final size distribution is centered around a value proportional to ratio of dispersed phase volume to solid particle mass. We plot the relationship between the mean droplet diameter and particle concentration for emulsions of ethylene glycol in chlorobenzene in Fig. 5.1A. From these data, together with estimates of the particle size and density, we also approximate the areal density of the adsorbed particle layer as $9 \cdot 10^{-3}\,\mathrm{nm}^{-2}$, which is consistent with a densely packed monolayer.

We use this limited coalescence process to produce emulsions with well defined droplet size and volume fraction by agitation alone. To do this we add precisely measured masses of chlorobenzene, particle dispersion, and ethylene glycol to polyethylene vials, seal them, and use a vortex mixer to homogenize the emulsion. The densities of the two fluids are nearly identical, but we still need to correct for the 4 vol. % solubility of chlorobenzene in ethylene glycol to arrive at accurate volume fractions. The solubility of ethylene glycol in chlorobenzene is much smaller, and thus a negligible correction to ϕ, but we still protect the droplets from Ostwald ripening by dissolving 0.5 wt % sorbitol in the ethylene glycol. For example, to prepare 15 g of an emulsion

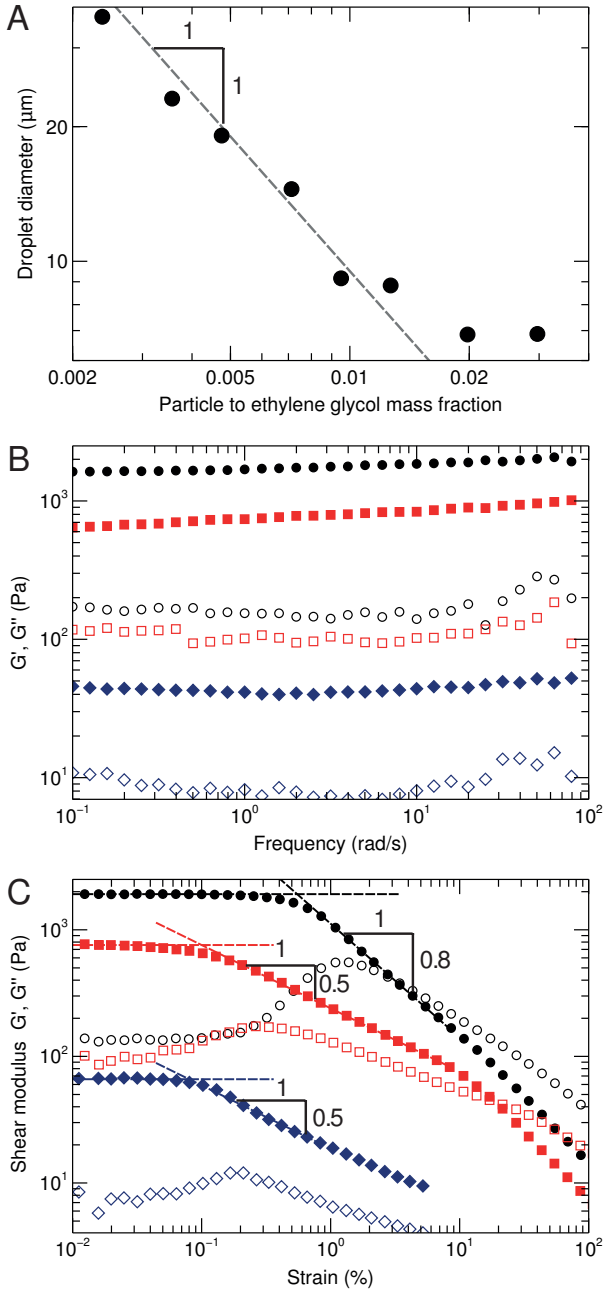

Figure 5.1: (A) Scaling of droplet diameter with silica particle to ethylene glycol mass ratio. (B) Swept frequency measurements of in-phase (G', filled) and out-of-phase (G", open) viscoelastic moduli of emulsions with volume fractions: 0.62 (diamonds), 0.68 (squares), and 0.74 (circles). (C) Swept strain measurements of in-phase (G', closed symbols) and out-of-phase (G", open symbols) viscoelastic response of emulsions with volume fractions: 0.62 (diamonds), 0.68 (squares), and 0.74 (circles).

of 10 μm diameter droplets at ϕ=0.7 we combine 4.65 g of chlorobenzene, 250 mg of Tol-ST, and 10.1 g of the sorbitol solution in a 20 ml vial and agitate with the vortex mixer for several minutes. This simple procedure produces droplets as small as $\sim$8 μm and droplet volume fractions as large as 0.8: smaller droplets require stronger agitation, and higher volume fractions are not stable.

To study the shear rheology of these emulsions we use a stress controlled rheometer (AR G2, TA Instruments). We use a hydrophobized cone-plate geometry for samples with shear moduli larger than 100 Pa, and a single gap, recessed bottom Couette geometry otherwise. All measurements are carried out at 23°C and are preceded by a pre-shear sequence composed of a constant shear rate flow step, and oscillating ring-down step, and a zero torque relaxation step. The frequency dependence of the storage, G', and loss, G'', moduli for emulsions composed of 10 μm droplets dispersed at volume fractions of 0.62, 0.68, and 0.74 are presented in Fig. 5.1B. From these data it is clear that $G'(\phi)$ is essentially independent of frequency. To determine the linear viscoelastic moduli and the yield strain, γ_y, of these emulsions we perform oscillatory measurements at 2 rad/s with increasing strain amplitudes. We plot the elastic and viscous components of the first harmonic of the ratio of oscillatory stress to strain amplitude in Fig 5.1C. We obtain G' from the small amplitude plateau of the in-phase component, and define γ_y as the cross-over strain amplitude between the linear and non-linear regimes. We similarly define the yield stress, σ_y, as the in-phase component of the oscillatory stress measured at γ_y.

To determine the scaling properties of G' we prepared emulsions over a wide range of droplet sizes and concentrations and measured their elastic moduli. We

plot the volume fraction dependence of G' obtained for samples composed of 10 μm, 20 μm, and 40 μm diameter droplets in Fig. 5.2A. After normalizing these data by the surface energy density, $\frac{\sigma}{R}$, three features of the data become apparent: $G'(\phi, R)$ is proportional to $\phi\,(\phi - \phi_c)$; in the compressed regime, $G'(\phi, R)$ scales with R^{-1}; finally, though solid-like behavior extends to volume fractions slightly below that of randomly closed packed spheres, the liquid to solid transition occurs at a critical $\phi_c \simeq 0.6$. These normalized shear moduli are presented in Fig 5.2B. These three features are all shared by surfactant stabilized emulsions, yet the magnitude of G' for emulsions composed of solid stabilized drops is nearly twelve times larger than that of an equivalent, surfactant stabilized formulation.

Surprisingly, though the shear modulus of Pickering emulsions is extraordinarily large, the stress required to yield them is not. Rheological measurements of surfactant-stabilized foams and emulsions have shown that both the shear modulus and the yield strain vanish at ϕ_c, with $\gamma_y \simeq \frac{\phi - \phi_c}{2}$. The yield stress of surfactant-stabilized emulsions thus scales as $\sigma_y \simeq \frac{\sigma}{2\,R}\,\phi\,(\phi - \phi_c)^2$, and values of the normalized yield stress, $\frac{\sigma_y\,R}{\sigma}$, measured from different samples collapse onto a universal curve. Pickering emulsions are not necessarily held to this universal behavior, as the properties of the adsorbed particles could well affect their non-linear elasticity; nevertheless, we find that the normalized yield stresses measured for our samples agree remarkably well with the relation that describes the normalized yield stress of surfactant-stabilized emulsions, as shown if Fig. 5.2C. Evidently, the adsorbed nanoparticles increase the stiffness of the emulsion, but render the solid remarkably fragile.

The adsorbed particles also drastically modify the plastic behavior of these emul-

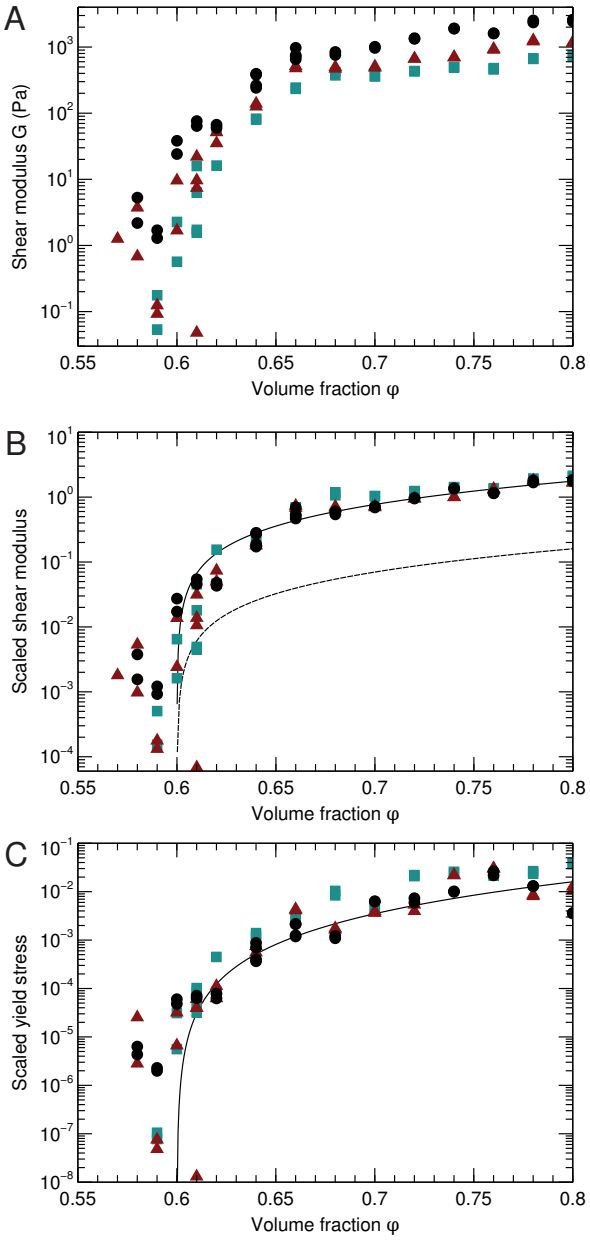

Figure 5.2: (A) Volume fraction dependence of the linear shear modulus, G, of emulsions composed of 10 μm (diamonds), 20 μm (triangles), and 40 μm (squares) droplets. (B) Volume fraction dependence of $\frac{GR}{\sigma}$ for same emulsions. Dashed line corresponds to the scaling of $\frac{GR}{\sigma}$ for surfactant-stabilized emulsions. Solid line is a rescaling of this result by $\frac{\tilde{\sigma}}{\sigma}$. (C) Volume fraction dependence of the normalized yield strain, $\frac{\sigma_y R}{\sigma}$, for same emulsions. Solid line corresponds to the scaling of $\frac{\sigma_y R}{\sigma}$ for surfactant-stabilized emulsions.

sions. For repulsive, surfactant-stabilized emulsions compressed beyond ϕ_c, G' scales like γ^{-2} for large oscillatory strains. As the volume fraction increases, the sharpness of the transition between the linear and non-linear regimes sharpens, but the scaling exponent remains the same. By contrast, the scaling of G' with strain amplitude for these solid-stabilized emulsions is much weaker. For $\phi \lesssim 0.7$, the value of G' in the non-linear regime scales as $\gamma^{-1/2}$. The steepness of this decay increases as ϕ increases, but does not decay faster than γ^{-1}, as shown if Fig. 5.1C. The rapid decline in the elastic response of surfactant-stabilized emulsions reflects the irreversible rearrangement of droplet contacts and positions. The narrower linear regime and substantially slower decay of the elasticity of Pickering emulsions suggests that the solid particles form a rigid structure that yields even before the droplet contacts are forced to break; however, the response of this kind of rigid structure to compression and shear could be substantially different.

To measure the bulk modulus of solid-stabilized droplets we replace the chlorobenzene with toluene and use X-ray attenuation imaging to measure the density of a quiescent droplet pile. When the contacts between the droplets and the walls are frictionless, every layer of the sediment must support the weight of all the droplets above it: generating a nearly constant stress gradient. The accumulation of stress forces droplets deeper into the sediment to pack more closely and expel more of the interstitial fluid. This gradient in the fluid fractions affects the transmission of X-rays through the sample, and the depth dependence of the volume fraction is reflected in the depth dependent attenuation. By replacing the chlorobenzene with toluene we increase the X-ray contrast between the fluids and strengthen the pres-

sure gradient. The density difference between the continuous and dispersed phases is $\delta\rho \simeq 250\,\mathrm{kg/m^3}$. As with the chlorobenzene, the ethylene glycol absorbs 3.5 vol. % of toluene, and the emulsification process for this alternate formulation is identical to that of the chlorobenzene/ethylene glycol mixture. Droplets obey the same limited coalescence process, and the dependence of the droplet size with added nanoparticle mass is the same. We find that these droplets are attractive at room temperature, but that this attraction disappears above 30°C. We perform oscillatory shear rheology measurements on such toluene based emulsions for $\phi > 0.7$ at 23°C and 35°C, and find that measurements of $\frac{GR}{\sigma}$ performed at high temperature agree with those measured in chlorobenzene. The large density difference between the fluids, however, precludes accurate measurements of this ratio for at lower volume fractions.

We use a microfocus CT scanner (HMX ST 225, Nikon Metrology) with a silver reflection target as the X-ray source and detector. The electron gun produces a focused beam of electrons that strike the silver target with an energy of ## keV: producing monochromatic Kα and broadband Bremsstrahlung radiation. This radiation is attenuated by the beryllium gun window, and filtered by a metal foil composed of 75 μm of palladium and 100 μm of aluminum. The additional metal filter significantly reduces the intensity of the radiation that strikes the sample, but improves the accuracy of our density measurements by selectively absorbing radiation with energies far removed from the Kα emission lines. Without a perfectly monochromatic source, density measurements derived from samples with large attenuation can be misleading. We minimize this effect by using samples no thicker than 3/8 in. and avoiding glass and other dense materials. We hold our samples in pieces of high precision, nylon

bushing stock with 1/4 in. inner and 3/8 in. outer diameters that are cemented to a glass platform, sealed, and loaded into the scanner.

To obtain quantitative concentration profiles we: sequentially load and record the same nylon container with toluene saturated ethylene glycol, ethylene glycol saturated toluene, and a sedimented and aged emulsion sample; compute transmitted intensities along the midpoint of each tube from processed images like the one shown in Fig. **??**A; compute the droplet volume fraction profile from the ratio of the difference in optical density (OD) between the emulsion sample and pure toluene to the OD difference between ethylene glycol and toluene, $\phi(z) = \frac{\mathrm{OD}_{em}(z) - \mathrm{OD}_{tol}(z)}{\mathrm{OD}_{eg}(z) - \mathrm{OD}_{tol}(z)}$; integrate $\phi(z)$ to obtain the pressure profile, $\Pi(z) = \delta\rho\, g \int_0^z \phi(z')\, \mathrm{d}z'$; eliminate z from $\Pi(z)$ with the measured $\phi(z)$. To avoid trapping air bubbles in the emulsion we first load 200 μL of toluene into the cleaned tube, add 1 mL of emulsion sample, degas in an evacuated desiccator. When the volume fraction close to the bottom of the tube will be significantly larger than ϕ_c we add an additional 10% of nanoparticles to the emulsified sample. We allow emulsion samples to age for two days at 37°C to dissolve the droplet gel and allow the emulsion to settle and consolidate.

We find that the bulk modulus of the solid-stabilized emulsions is no larger than that of surfactant-stabilized emulsions. Previous experiments have shown that the osmotic pressure and shear modulus of surfactant-stabilized emulsions are nearly identical, and thus $\Pi(\phi) \simeq \frac{\sigma}{R}\, \phi\, (\phi - \phi_c)$ We measure $\phi(z)$ for a sedimented emulsion composed of 30 μm diameter droplets, and present the data in Fig. 5.3B. We use these data to compute $\Pi(\phi)$, and obtain an effective interfacial tension σ_{eff} by fitting the low pressure range of these data to the form determined for surfactant-stabilized emul-

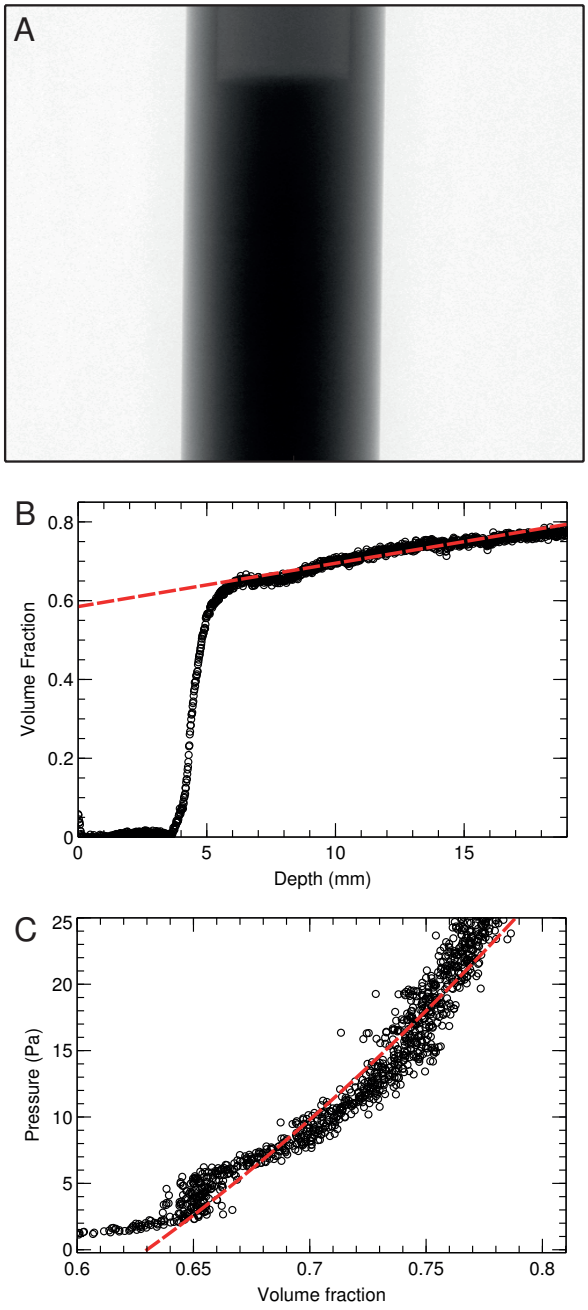

Figure 5.3: (A) Image of X-ray attenuation for a sedimented emulsion composed of 20 μm droplets, contained in a nylon tube. (B) Depth dependence of the droplet volume fraction derived from X-ray attenuation images. Dashed line is a guide to the eye. (C) Volume fraction dependence of the osmotic pressure, $\Pi(\phi)$, derived from the quiescent volume fraction profile. Dashed line is a fit of $\Pi(\phi)$ to the equation of state of surfactant stabilized emulsions.

sions, as shown in Fig. 5.3C. Measured in this way, we obtain a value $\sigma_{eff} \simeq 3\,\mathrm{mN/m}$, which is only one third as large as the tension measured from the pure fluids: consistent with a positive surface pressure exerted on the interface by repulsive particles that reduces the tension of the fluid interface. However, if the true interfacial tension of our particle laden interface is $3\,\mathrm{mN/m}$, the apparent interfacial tension $\tilde{\sigma}$ is then nearly 40 times larger than the equilibrium value. Moreover, for $\phi > 0.65$, the bulk modulus $K \simeq \phi_c^2 \frac{\sigma}{R} \simeq 100\,\mathrm{Pa}$, is smaller than G, and the ratio $K/G \ll 1$ for $\phi > 0.7$: the Poisson's ratio of this material is thus negative even for modest compressions.

The effects of adsorbed particles on the mechanical properties of emulsions are fascinating. The provide remarkably strong resistance to small shear strains, and fundamentally alter the plastic behavior of the material, but offer almost no resistance to compressive strains. This behavior appear consistent with a stiff but fragile elastic shell formed by the particles under two-dimensional compressive tension. This film may jam under small deformations of the interface that do not increase its area, but become fluidized by more isotropic deformations that increase the free volume of the bound particles. This interfacial jamming thus couples the yielding of the interface to the yielding of the droplet contact network and produces an incredibly stiff yet fragile material that can have strongly negative Poisson's ratios.

Chapter 6

Particle-packed foams for enhanced dissolution of pharmaceutical actives

Pharmaceutical compounds that are administered orally but are meant to enter the bloodstream must dissolve quickly so that they may be absorbed and become bioavalable before excretion. However, for nearly 40 % [28] of marketed drugs and nearly 90 % of drug candidates [4], hydrophobicity significantly hinders their dissolution and thus their bioavailability. Moreover, without an adequate formulation, the absorption of these compounds can be erratic; large variations in the absorbed dose for drugs with a narrow therapeutic window can cause toxicity [9, 92]. Formulations capable of delivering such hydrophobic compounds effectively are therefore essential to their development and commercialization.

A general and direct way to improve dissolution rates is to increase the surface-

to-volume ratio of the active by making nanoparticles. For many actives, precipitation of crystalline nanoparticles from solution is an inexpensive and effective way to accomplish this. Large quantities of nanoparticles can be produced by precisely balancing the nucleation, growth, and colloidal stability of crystals in a supersaturated solution of the active [36]. However, the processing parameters of each compound must be optimized independently, and restrictions in achievable mixing rates and admissible solvents and stabilizers limit the smallest practicable particle size for many compounds [80]. Particles with diameters of a few hundred nanometers can also be produced by wet media milling. This physical attrition process is compatible with a wide range of compounds, including several commercially available formulations [64, 66]. However, particle production can require days of intense agitation and generates large amounts of heat: This makes this process unsuitable for compounds that melt or degrade in the hot slurry; this also complicates large scale production [31, 69].

It is also possible to increase the dissolution rate of hydrophobic drugs by blending them with hydrophilic polymers. By avoiding crystallinity altogether, amorphous solid solutions of this kind improve the bioavailability of a remarkably wide range of compounds using just a few polymeric carriers [17, 18, 23]. Nevertheless, it is still necessary to extend their applicability and find new methods to increase the efficacy of existing polymeric formulations. Some of this may be accomplished by designing new polymeric carriers [57], but these must undergo extensive and costly safety testing; by contrast, physical transformations that change the particle size or surface area of existing formulations can be implemented quickly, as they do not affect the safety of the material itself.

Here we demonstrate that it is possible to double the dissolution rate of the active contained in a polymeric solid solution by including an additional supercritical foaming step before milling. This additional step produces a low density foam with micrometer scale bubbles that are separated by films 10–20 nm thick. Furthermore, it is possible to quadruple the dissolution rate of the original formulation by homogeneously blending inert silica nanoparticles into the solid solution prior to foaming. This simple physical transformation combines the benefits of the amorphous formulation and nanometer scale confinement, is compatible with large scale pharmaceutical production, and can quadruple the dissolution rate of a state-of-the-art solid solution.

6.1 Milled solid solutions

The dissolution of compounds blended into a solid solution can be quite complex [20, 45]. Solid solutions are typically coarsely ground or spray dried into powders before being pressed into tablets; yet, though smaller particles may be expected to release active faster, the precise effects of particle size and surface area are not obvious. We determine this relation for our formulation by measuring the dissolution rate of sieved fractions of a milled powder under sink conditions.

We thus prepare a solid solution of 20 % w/w clotrimazole in poly(N-vinyl pyrrolidone-co-vinyl acetate) (PVPVA), gently cryo-mill this blend into 10–100 μm pieces, and sieve and separate the resulting powder by particle size. Finally, we add a small amount of each fraction to a stirred cell and monitor the concentration of dissolved drug by UV absorbance: such dissolution measurements have been shown to correlate with *in vivo* bioavailability [1, 24, 25]. The concentration of drug is kept below

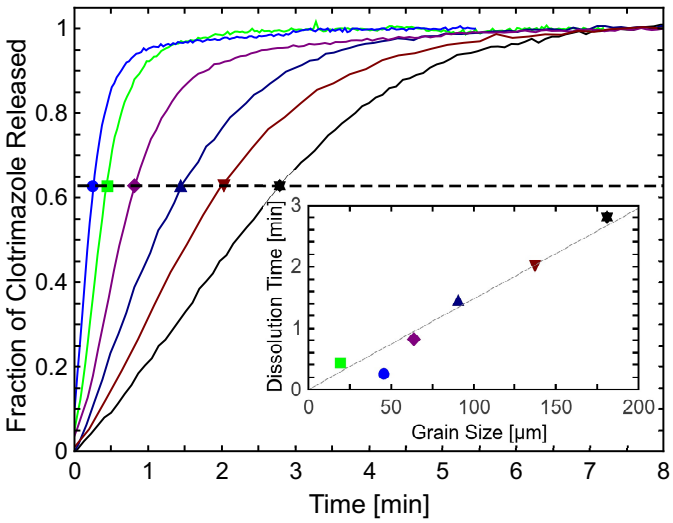

Figure 6.1: Clotrimazole release measurements for sieved solid solution powders. Traces show amount of drug released with time for a sequence of particle sizes increasing from left to right. (Inset) Plot of mean particle size and corresponding dissolution times, defined as the time required to dissolve 63 % of the active, for measured powder size fractions. Colored symbols identify dissolution traces with corresponding dissolution times.

saturation to ensure sink conditions and avoid recrystallization. These measurements produce traces of the amount of mass dissolved as a function of time for each size fraction, from which we extract a dissolution time, τ: defined as the amount time required to dissolve 63 % of the active.

The resulting data show that dissolution times for this combination increase linearly with particle size, as plotted in Fig. 6.1. This simple linear scaling is consistent with carrier controlled dissolution [49], whereby the dissolution of the active is limited by the dissolution of the matrix polymer, with an erosion rate of $\sim$10 μm/min.

6.2 Foamed solid solutions

The surface area of a polymeric solid solution can be increased dramatically by simple and inexpensive supercritical foaming processes [3, 41, 85]. The extrusion process used to make commercial microcellular polymer foams extends the hot melt extrusion process used in commercial production of solid solutions without compromising pharmaceutical safety [89]. We employ a batched, autoclave process that exposes the polymeric solid solution to supercritical CO_2. At high CO_2 pressure the gas diffuses into the blend, which swells the polymer and depresses its glass transition temperature, T_g. A rapid drop in pressure then induces an immediate phase separation through nucleation and growth of bubbles. As the CO_2 demixes and the bubbles expand, the T_g of the polymer increases and its internal temperature decreases. The expansion of the bubbles stops when the matrix vitrifies and the light, porous foam structure is quenched. Finally, gentle milling is enough to break this structure into small pieces. This process is schematically summarized in Fig. 6.2.

To produce foams with nanoscale features using the autoclave process we first optimize the choice of matrix material, operating pressure and temperature, and pressure release rate [32, 68]. The PVPVA matrix used for the unfoamed solid solution is ideal for this process, as it dissolves greater than 20 % w/w of the actives we tested and has a high affinity for CO_2. To make foams with micrometer-scale bubbles, nanometer-scale films, and 90 % void volume fractions we set the CO_2 pressure to 400 atm, the depressurization time to ∼200 ms, and the chamber temperature to 40°C. The films of foams prepared under these conditions are tens of nanometers thick, almost two orders of magnitude smaller than the bubbles. However, the Plateau borders, the

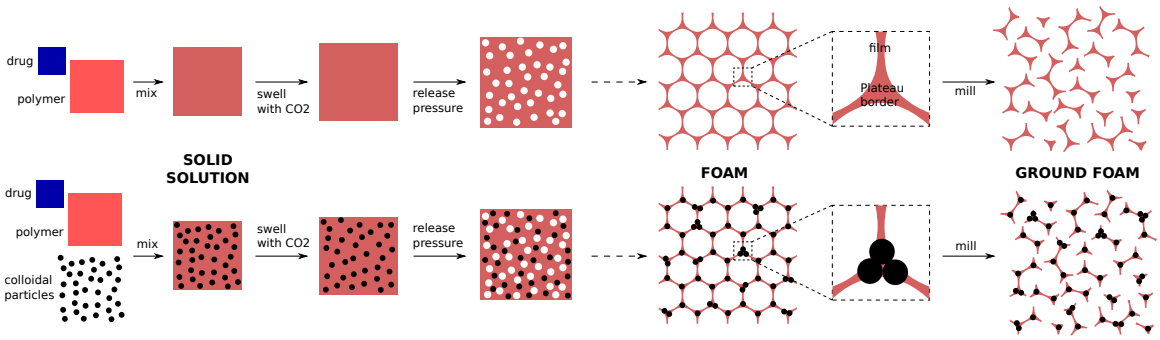

Figure 6.2: Schematic of the foam templating process. The polymer matrix is shown in yellow, drug molecules in blue, and colloidal particles in black. Drug molecules are dissolved in the polymer to produce a stable solid solution (green). Solid particles may also be added to the polymer matrix without altering other processing steps. High pressure CO_2 swells the solid solution, and rapid depressurization nucleates bubbles. The bubbles grow and pack until the matrix hardens, producing a porous and light foam. Solid particles, initially dispersed homogeneously, are excluded from the thin films and pack in the Plateau borders (see text).

space between three or more bubbles, are much thicker, as shown in Fig. 6.3A.

We use the same gentle milling procedure used for the unfoamed solid solution and find, surprisingly, that the grain size distributions for the foamed and unfoamed samples are the same, as shown in Fig. 6.4A. However, despite the gross similarity of the powders, Brunauer–Emmett–Teller (BET) nitrogen adsorption measurements [13] show a fifteen fold increase in surface area and electron micrographs of powder grains confirm that the milled foams retain their porous structure: as presented in Table 6.1 and Fig. 6.4B.

Finally, we perform stirred cell release measurements on whole powders of milled foamed and unfoamed solid solutions and find that foamed samples dissolve twice as fast as their unfoamed counterparts – the current benchmark for oral delivery. This doubling is evident from clotrimazole release measurements performed on whole powders of foamed and unfoamed samples, presented in Fig. 6.5. Similar results are

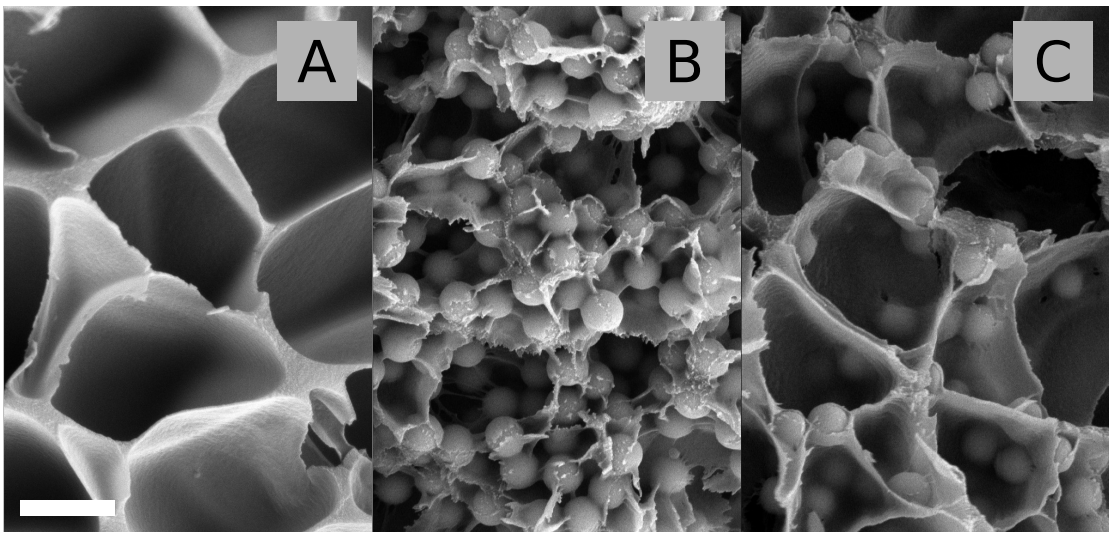

Figure 6.3: Scanning electron micrographs depicting the effect of unmodified silica particles on foams prepared at 400 atm, 40°C, with a ∼200 ms pressure release time. (A) Foam with no particles, (B) with 57% v/v hydrophilic silica particles, and (C) with 25% v/v hydrophilic silica particles. Scale bar is 1 μm wide. Particles loaded at 57 % reduce the bubble size and film thickness, and increase the density of the foam. At 25 % loading, particles accumulate in Plateau borders without disturbing the gross structure of the foam.

Sample	Specific Surface Area	
	m^2/g	m^2/cm^3
Unfoamed solid solution	0.5±0.1	0.6±0.1
Foamed solid solution	8.6±0.2	10.3±0.3
Foamed with 25 % hydrophilic particles	7.7±0.2	10.4±0.3
Foamed with 25 % poorly mixed particles	7.5±0.2	10.1±0.3
Foamed with 25 % hydrophobic particles	9.0±0.2	12.2±0.3

Table 6.1: Specific surfaces areas of samples measured by BET nitrogen adsorption.

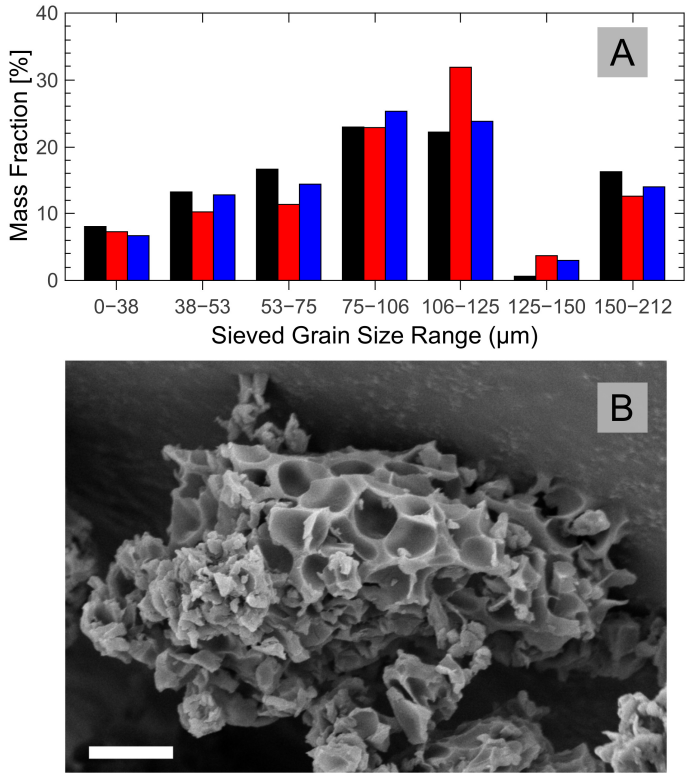

Figure 6.4: Results of the milling process. (A) Grain size distributions for powders of unfoamed solid solutions (black), foamed solid solutions (red) and foamed solid solutions with colloidal particles (blue) after milling. (B) Scanning electron micrograph of a milled foam grain. Scale bar is 3 μm wide.

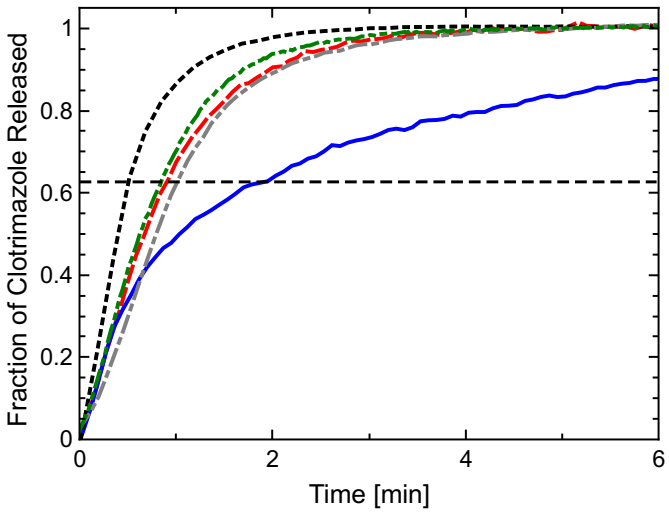

Figure 6.5: Timed release measurements for formulations with clotrimazole in 10 mM SDS solution. The baseline, unfoamed solid solution (—) is compared to: foamed solid solution without added particles (– –); foamed solid solution with 25 % v/v hydrophilic particles (- - -); foamed solid solution with 25 % v/v hydrophobic particles (– -); foamed solid solution with 25 % v/v poorly-dispersed hydrophilic particles (– - –). The initial dissolution rate of foamed solid solutions with hydrophilic particles is 1.8 times faster than the foamed sample without particles, and 3.8 times faster than the unfoamed solid solution.

obtained for itraconazole, fenofibrate, carbamazepine, and cholesterol, but the finite transit time to the spectrometer and their faster dissolutions makes it difficult to resolve some of the differences.

Although a doubling of the dissolution rate is a large enhancement over the current state-of-the-art, the improvement is clearly not proportional to the 15-fold increase in surface area produced by foaming. Closer inspection of the foam morphology reveals that even in the lowest-density samples the Plateau borders are ∼10 times thicker than the films, as shown in Fig. 6.3A. By modeling the Plateau borders as cylinders and the films as sheets assembled in a close-packed polyhedral structure, we estimate that the total volume in the Plateau borders is twice as large as that of the films. So,

while the films dominate the surface area of the material, most of the active is locked in the larger Plateau borders. We cannot further reduce the size of these features by changing the processing parameters, so we need a fundamentally different method to control the structure of the foam.

6.3 Foamed solid solutions with solid particles

Though our foaming process cannot produce much smaller bubbles, producing inert, solid particles with a diameter comparable to 100 nm is straightforward. Moreover, instead of being limited to Plateau borders a ~ 100 nm thick, the length scale of the pores in a dense packing of such particles is closer to tens of nanometers. Densely packing such particles into the Plateau borders of the foam could reduce the amount of material in these regions and provide further confinement; however, it is not obvious that our far from equilibrium foaming process should yield such an ordered structure. Nevertheless, we find that silica particles too large to fit into the films between bubbles can alter the foam morphology dramatically.

In foams made from a 57 % v/v blend of 380 nm silica particles and polymer, the particles appear to join adjacent films, acting as effective Plateau borders. The mean size of the bubbles is smaller, and the void fraction is reduced. Nevertheless, the reduction in the polymer feature size is striking; the films in these materials are less than 10 nm thick – thinner than for any other foam we have made – and the Plateau borders are replaced with particles coated in a thin film of polymer, as shown in Fig. 6.3B.

Decreasing the particle loading to 25 % v/v dilutes the amount of active in the structure less, yet still provides enough particles to seemingly fill the Plateau borders. Electron micrographs, foam density measurements, and nitrogen adsorption measurements show that the bubble sizes, void volume fractions, and specific surfacea areas of these samples are the same as those of unfilled foams, as shown in Table 6.1 and Fig. 6.3C. Even the grain size distrubution after cryomilling is indistinguishable from the other samples, as shown in Fig. 6.4A. Based on such bulk properties alone, one might not expect a significant change in the dissolution rate; yet, surprisingly, stirred cell release measurements show that clotrimazole carried by foams with 25 % v/v solid particles dissolves twice as fast as that in foams without added particles, and four times as fast as that in unfoamed solid solutions, as shown in Fig. 6.5.

As the bulk properties of filled and unfilled foams are essentially the same, the faster dissolution rate of filled foams must be due to some other effect of the added particles. Electron micrographs show that the structure of the Plateau borders in these filled foams is fundamentally different from those of unfilled foams: particles accumulate exclusively in the Plateau borders and reduce them to a network of ∼20 nm thin films joining adjacent solid particles, shown in Fig. 6.3C. This efficient, hierarchical packing of particles and bubbles is made possible by the large difference between the sizes of the two types of inclusions; while the soft, deformable bubbles occupy the most space and confine material into thin films, the smaller particles are excluded from the films and fill thickest regions of the foam without disturbing the gross morphology. If this improvement is due to the disruption of the Plateau borders by silica particles that are otherwise inert, adding particles without affecting most Plateau

borders should remove the improvement.

To test this hypothesis we develop two approaches to add particles that leave most Plateau borders intact. First, we simply mix the particles poorly when adding them to the polymer. We find that the resulting foams contain some dense clusters of particles, but the Plateau borders outside these clusters remain untouched. Second, we make solid solutions with hydrophobically modified silica particles. Whereas unmodified silica particles are engulfed by the polymer, hydrophobically modified particles protrude from it and leave most of the Plateau borders unperturbed. Electron micrographs of foams showing the complete wetting of the unmodified particles by the polymer, the agglomeration of the poorly mixed particles, and the dewetting and bunching of the hydrophobically modified particles are shown in Fig. 6.6. In all cases, the bubble sizes, densities, and specific surface areas measured by nitrogen adsorption remain similar; the surface area of foams with hydrophobic particles is slightly larger, perhaps due to a contribution from expelled particles.

After following the same milling and dissolution process as before we find that removing the ability of particles to fill the Plateau borders uniformly removes the enhancement to the dissolution rate. Measurements of clotrimazole release for all four foamed structures and for the unfoamed solid solution – the current benchmark for oral delivery – show the increased dissolution rate brought upon by foaming, the additional increase provided by uniformly adding wetting particles, and the loss of function in foams where the packing of particles in the Plateau borders has been hindered. These data are presented in Fig. 6.5. The increased dissolution rate of foams with well-mixed, hydrophilic silica particles is thus due to a purely geometrical

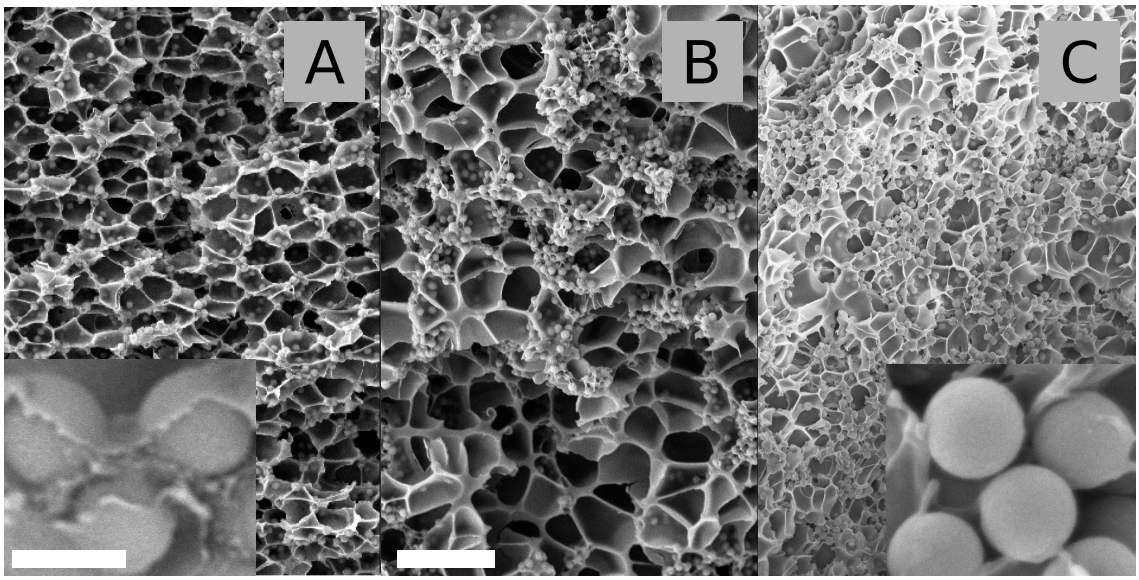

Figure 6.6: Electron micrographs depicting the effect of changing particle wettability and homogeneity on the Plateau borders of foams prepared at 400 atm, 40°C, with a ∼200 ms pressure release time. All samples contain 25 % v/v colloidal particles in polymer. (A) Foams with well-dispersed hydrophilic particles, (B) foams with poorly-dispersed hydrophilic particles, and (C) foams with hydrophobic particles. Scale bar is 5 μ wide. Homogeneity of mixing and surface modification changes distribution of particles (see text). Insets show magnified views of polymer (A) wetting unmodified silica particles or (C) expelling hydrophobically modified particles. Inset scale bar is 500 nm wide.

effect: the efficient packing of particles and bubbles reduces the thickest structure in the foam to a network of quickly dissolving thin films.

6.4 Conclusions

The hierarchical confinement of solid solutions of active to nanoscale films dramatically increases the dissolution rate of poorly soluble pharmaceuticals. The addition of solid particles to the polymeric matrix leads to foams where the largest gaps between micron-sized bubbles are spontaneously filled and where the active laden material is confined to nanoscale films throughout the foam. This structural effect can be achieved through a simple, scalable physical process that enhances the functionality of a state-of-the-art formulation, the solid solution. Although particularly suited for pharmaceutical actives with low water solubility, the process is general and can be extended to other actives, polymers, and particles.

6.5 Materials

All materials were used as received: PVPVA, poly(1-vinylpyrrolidone-co-vinyl acetate) 6:4, (Kollidon VA 64, BASF, CAS 25086-89-9); CO_2 , Carbon Dioxide (Coleman Grade - Min. Purity 99.99 % Liquid Phase); 380 nm silica particles (Angstromsphere Monodisperse Silica Powder, Fiber Optic Center Inc., SIO2P025-01); Clotrimazole (Selectchemie, Lot No. 20051116); Itraconazole (Selectchemie, Batch No. IT0070709); Fenofibrate (Aldrich, Batch No. 017K1401); Carbamazepine (Pfannenschmitt, Batch No. 07092639); Cholesterol (Alfa Aesar, 96% pure, CAS 57-88-5).

6.5.1 Hydrophobic silica preparation

To make hydrophobic particles 30 g of hydrophilic silica particles are first dispersed in 30 ml ethanol by ultrasonication. We then add 90 g of eicosanol and heat the mixture to 90°C under vacuum to remove the ethanol. After completely removing the ethanol we heat to 180°C under nitrogen and stir overnight. We clean the particles by redispersion and centrifugation (5 times) in a chloroform/hexane mixture, 1:1 by volume, and dry them under reduced pressure.

6.5.2 Preparing solid solutions

We employ two methods to prepare solid solutions of active in polymer. When small amounts are needed we use a co-solvent blending method, whereby the active and polymer are dissolved in a common solvent, either acetone or ethanol, which is removed by evaporation. To completely remove the solvent we first dry the solid solution in an oven at 50°C overnight, mill, and dry again. The resulting powders are tested for residual solvent on a thermogravimetric analyzer (TGA, TA Instruments Q5000IR) and a differential scanning calorimeter (DSC, TA Instruments Q200). Fully dried samples show no significant loss of weight upon heating, show a single glass transition temperature, and show no melting endotherm. To form bulk pellets the powders are heated to 120°C and pressed within a die (Carver 24-ton hydraulic press). To prepare solid solutions with solid particles we first disperse the particles in the co-solvent, add the polymer and drug, dry, and finally press into a pellet.

For larger amounts of sample (∼10 g) we use hot melt extrusion. We directly mix polymer and drug in a small-scale twin-screw extruder (Micro Compounder, DACA

Instruments) at a temperature well above either the melting point of the drug or the glass transition of the polymer. For clotrimazole we perform the extrusion at 160°C. We use high performance liquid chromatography(Agilent 1100 HPLC) to test for degradation of the drug and operate at temperatures below which degradation is measurable. To prepare solid solutions with solid particles using this method, we combine powders of polymer, active, and particles and extrude them as described above.

To make solid solutions with poorly-dispersed particles we first mill a pre-made solid solution, combine the resulting powder with powdered silica particles, mix gently and melt-press to make the final pellets.

The mixing ratio of drug to polymer is 1:4 by weight for all formulations. The addition of solid particles thus reduces the loading of active in the final composites.

6.5.3 Foaming

Solid solutions and composites are foamed using a custom-built apparatus. Gas is first drawn from a cylinder filled with liquid CO_2 by a high pressure syringe pump (model 260D, Teledyne Isco, Lincoln NE) that is connected to a 100 ml steel autoclave (Pressure Products Industries Inc., Warminster, PA, purchased from Supercritical Fluid Technologies Inc., Newark, DE). The pump is then disconnected from the cylinder and fluid is transfered to the autoclave at the operating pressure. The operating temperature of the autoclave is set by a PID controller (Omega Engineering, CSI32K iSeries Benchtop controller), acting upon an electric heater with feedback from a thermocouple mounted inside the chamber (Omega Engineering, KHSS-18G-

RSC). The pressure release time is minimized by reducing the amount of dead volume in the chamber and venting the CO_2 through a pneumatically actuated 3-way valve (Swagelok, SS-H83XPF2-53S). The apparatus is capable of pressures as high as 500 atm, and temperatures as high as 200°C, with pressure release times as short as 100 ms. In a typical experiment, 1 gram of solid solution is added to the chamber and allowed to soak for 4 hours at 40°C and 400 atm pressure. The pressure is then released within 200 ms.

6.5.4 Choice of polymer

Polymeric carriers for foamed solid solutions must be good solvents for the target molecule, must have high affinity for CO_2, must be amorphous and have a T_g low enough to be fluid under pressure but solid at room conditions, and must dissolve quickly in water.

We use a pharmaceutically approved, random copolymer of vinyl pyrrolidone (VP) and vinyl acetate (VAc). The VP:VAc monomer weight ratio is 3:2, with an Mn of 15 Kg/mol and a polydispersity index of ∼3. The VAc comonomer increases the polymer's CO_2 affinity and reduces it T_g, while the VP comonomer provides water solubility and solvency for many drugs [53]. The relatively low molecular weight of the polymer reduces the melt viscosity and increases its dissolution rate. The glass transition temperature of the pure copolymer is 108°C, above the critical point of CO_2 but well below the maximum working temperature of our apparatus. Actives dissolved in the polymer typically alter the T_g of the blend [19], which can be compensated for by adjusting the temperature of the foaming process.

6.5.5 Imaging

We use a Zeiss Ultra55/Supra55VP field emission scanning electron microscope (FESEM) to image the foam samples. To image the interior of the structure without damaging it, we first plunge the foam into liquid nitrogen and fracture it with a sharp blade. We sputter-coat a thin layer of platinum/palladium to reduce charging under the electron beam and improve image quality.

6.5.6 Milling and characterizing

Samples are loaded into a liquid nitrogen cooled, 50 ml stainless-steel jar together with one 25 mm stainless steel ball and milled for 2 minutes at 10 Hz (CryoMill, Retsch Corp.) The surface areas of the milled samples are measured by nitrogen adsorption using the BET method (Beckman Coulter Surface Area Analyzer SA3100). We measure the size distribution of the grains, by sieve fractionation through a stack of stainless steel sieves (ASTM E-11 standard) using a Cole Parmer Sieve Shaker vibrating at 60 Hz with 1 s tapping. The grain size distribution is then determined by weighing the contents of each sieve fraction after 20 minutes operation.

6.5.7 Timed release measurements

We measure we concentration of active dissolved with time using a custom-built apparatus consisting of a dissolution chamber, a peristaltic pump, and a UV-VIS spectrophotometer. Fluid is drawn out of the dissolution chamber (Millipore Solvent-Resistant Stirred Cell 76 mm) and through a quartz flow cell (Starna Cells) mounted in the UV-VIS spectrophotometer (Perkin Elmer Lambda 40) by the peristaltic pump.

The bottom of the chamber is fitted with a filter membrane (Sterlitech PTFE laminated membrane, with either a 0.2 or 0.45 μm pore size) that prevents undissolved particles from reaching the spectrophotometer. The dissolution chamber has a stir bar that is actuated by a magnetic stir-plate from below. The solution is continuously flowed through the flow cell while the spectrometer records the instantaneous absorbance. The optical density as a function of drug content is calibrated using a concentration series prepared in a good solvent.

After the fluid exists the spectrometer cell it reaches the peristaltic pump and is recirculated back into the chamber, keeping the total volume constant. The transit time between the chamber and the spectrometer, defined as the total delay time between the addition of a well mixed sample to the chamber and the appearance of a steady signal on the spectrophotometer, is approximately 30 seconds. This sets the time resolution of the measurement.

Before the samples are added to the dissolution chamber, they are mixed with an inert spacer to prevent aggregation and improve wetting: either microcrystalline cellulose (20 μm powder, Aldrich) or fumed silica (CAB-O-SIL M5, Cabot Corp.). These mixed powders are then added directly into the dissolution chamber. The choice of spacer did not affect the measured dissolution rate.

Bibliography

[1] Gordon L. Amidon et al. "A Theoretical Basis for a Biopharmaceutic Drug Classification: The Correlation of in Vitro Drug Product Dissolution and in Vivo Bioavailability". In: *Pharm Res* 12.3 (Mar. 1995), pp. 413–420. ISSN: 0724-8741, 1573-904X. DOI: 10.1023/A:1016212804288. URL: http://link.springer.com/article/10.1023/A:1016212804288.

[2] S. Arditty et al. "Interfacial properties in solid-stabilized emulsions". In: *The European Physical Journal B* 44.3 (Apr. 2005), pp. 381–393. ISSN: 1434-6028, 1434-6036. DOI: 10.1140/epjb/e2005-00137-0. URL: http://www.springerlink.com/index/10.1140/epjb/e2005-00137-0.

[3] Kelyn A. Arora, Alan J. Lesser, and Thomas J. McCarthy. "Preparation and Characterization of Microcellular Polystyrene Foams Processed in Supercritical Carbon Dioxide". In: *Macromolecules* 31.14 (July 1998), pp. 4614–4620. ISSN: 0024-9297. DOI: 10.1021/ma971811z. URL: http://dx.doi.org/10.1021/ma971811z.

[4] Leslie Z. Benet, Chi-Yuan Wu, and Joseph M. Custodio. "Predicting Drug Absorption and the Effects of Food on Oral Bioavailability". In: *Influence of Lipid Excipients on Oral Drug Absorption*. Vol. 99. Bulletin Technique Gattefossé. Gattefossé, 2006, pp. 9–16.

[5] Ludovic Berthier and Thomas Witten. "Glass transition of dense fluids of hard and compressible spheres". In: *Physical Review E* 80.2 (Aug. 2009). ISSN: 1539-3755, 1550-2376. DOI: 10.1103/PhysRevE.80.021502. URL: http://link.aps.org/doi/10.1103/PhysRevE.80.021502.

[6] Jerome Bibette, Veronique Schmitt, and Fernando Leal-Calderon. *Emulsion science: basic principles*. English. New York; London: Springer, 2007. ISBN: 9780387396828 0387396829.

[7] D. Bicout et al. "Depolarization of multiply scattered waves by spherical diffusers: Influence of the size parameter". In: *Phys. Rev. E* 49.2 (Feb. 1994), pp. 1767–1770. DOI: 10.1103/PhysRevE.49.1767. URL: http://link.aps.org/doi/10.1103/PhysRevE.49.1767.

[8] Maurice A. Biot. "General Theory of Three-Dimensional Consolidation". In: *Journal of Applied Physics* 12.2 (1941), p. 155. ISSN: 00218979. DOI: 10.1063/1.1712886. URL: http://link.aip.org/link/JAPIAU/v12/i2/p155/s1&Agg=doi.

[9] Stephanie Bosselmann and Robert O. Williams. "Route-Specific Challenges in the Delivery of Poorly Water-Soluble Drugs". In: *Formulating Poorly Water Soluble Drugs*. AAPS Advances in the Pharmaceutical Sciences Series 3. AAPS Press, 2012. ISBN: 978-1-4614-1144-4. URL: http://www.springer.com/biomed/pharmacology+&+toxicology/book/978-1-4614-1143-7.

[10] G. Brambilla et al. "Probing the Equilibrium Dynamics of Colloidal Hard Spheres above the Mode-Coupling Glass Transition". In: *Physical Review Letters* 102.8 (Feb. 2009). ISSN: 0031-9007, 1079-7114. DOI: 10.1103/PhysRevLett.102.085703. URL: http://link.aps.org/doi/10.1103/PhysRevLett.102.085703.

[11] L. Bressy et al. "Rheology of emulsions stabilized by solid interfaces". In: *Langmuir* 19.3 (2003), pp. 598–604. URL: http://pubs.acs.org/doi/abs/10.1021/la0264466.

[12] A. Brodin et al. "Light scattering and dielectric manifestations of secondary relaxations in molecular glassformers". In: *Eur. Phys. J. B* 36.3 (Dec. 2003), pp. 349–357. ISSN: 1434-6028, 1434-6036. DOI: 10.1140/epjb/e2003-00353-6. URL: http://link.springer.com/article/10.1140/epjb/e2003-00353-6.

[13] Stephen Brunauer, P. H. Emmett, and Edward Teller. "Adsorption of Gases in Multimolecular Layers". In: *J. Am. Chem. Soc.* 60.2 (Feb. 1938), pp. 309–319. ISSN: 0002-7863. DOI: 10.1021/ja01269a023. URL: http://dx.doi.org/10.1021/ja01269a023 (visited on 02/16/2014).

[14] P. T. Callaghan, M. A. Le Gros, and D. N. Pinder. "The measurement of diffusion using deuterium pulsed field gradient nuclear magnetic resonance". In: *The Journal of Chemical Physics* 79.12 (1983), p. 6372. ISSN: 00219606. DOI: 10.1063/1.445745. URL: http://link.aip.org/link/JCPSA6/v79/i12/p6372/s1&Agg=doi.

[15] Paul T. Callaghan. *Principles of Nuclear Magnetic Resonance Microscopy*. Oxford University Press, 1993. ISBN: 9780198539971.

[16] C. J. Cheng et al. "Hydrophobic Modification and Regeneration of Shirasu Porous Glass Membranes on Membrane Emulsification Performance". In: *Chemical Engineering & Technology* 31.3 (Mar. 2008), pp. 377–383. ISSN: 09307516, 15214125. DOI: 10.1002/ceat.200700353. URL: http://doi.wiley.com/10.1002/ceat.200700353.

[17] Win Loung Chiou and Sidney Riegelman. "Pharmaceutical Applications of Solid Dispersion Systems". In: *Journal of Pharmaceutical Sciences* 60.9 (1971), pp. 1281–1302. DOI: 10.1002/jps.2600600902. URL: http://onlinelibrary.wiley.com/doi/10.1002/jps.2600600902/abstract.

[18] Win Loung Chiou and Sidney Riegelman. "Preparation and dissolution characteristics of several fast-release solid dispersions of griseofulvin". In: *Journal of Pharmaceutical Sciences* 58.12 (1969), pp. 1505–1510. ISSN: 1520-6017. DOI: 10.1002/jps.2600581218. URL: http://onlinelibrary.wiley.com/doi/10.1002/jps.2600581218/abstract.

[19] P. R. Couchman and F. E. Karasz. "A Classical Thermodynamic Discussion of the Effect of Composition on Glass-Transition Temperatures". In: *Macromolecules* 11.1 (Jan. 1978), pp. 117–119. ISSN: 0024-9297. DOI: 10.1021/ma60061a021. URL: http://dx.doi.org/10.1021/ma60061a021.

[20] Duncan QM Craig. "The mechanisms of drug release from solid dispersions in water-soluble polymers". In: *International journal of pharmaceutics* 231.2 (2002), pp. 131–144. DOI: 10.1016/S0378-5173(01)00891-2. URL: http://www.sciencedirect.com/science/article/pii/S0378517301008912.

[21] J. Crassous. "Diffusive Wave Spectroscopy of a random close packing of spheres". In: *The European Physical Journal E* 23.2 (June 2007), pp. 145–152. ISSN: 1292-8941, 1292-895X. DOI: 10.1140/epje/i2006-10079-y. URL: http://www.springerlink.com/index/10.1140/epje/i2006-10079-y.

[22] Svetlana R. Derkach. "Rheology of emulsions". In: *Advances in Colloid and Interface Science* 151.1-2 (Oct. 2009), pp. 1–23. ISSN: 00018686. DOI: 10.1016/j.cis.2009.07.001. URL: http://linkinghub.elsevier.com/retrieve/pii/S0001868609000517.

[23] James C. DiNunzio et al. "Melt Extrusion". In: *Formulating Poorly Water Soluble Drugs*. AAPS Advances in the Pharmaceutical Sciences Series 3. AAPS Press, 2012. ISBN: 978-1-4614-1144-4. URL: http://www.springer.com/biomed/pharmacology+&+toxicology/book/978-1-4614-1143-7.

[24] Aristides Dokoumetzidis and Panos Macheras. "A century of dissolution research: From Noyes and Whitney to the Biopharmaceutics Classification System". In: *International Journal of Pharmaceutics* 321.1–2 (Sept. 2006), pp. 1–11. ISSN: 0378-5173. DOI: 10.1016/j.ijpharm.2006.07.011. URL: http://www.sciencedirect.com/science/article/pii/S0378517306005813.

[25] Jennifer B. Dressman et al. "Dissolution Testing as a Prognostic Tool for Oral Drug Absorption: Immediate Release Dosage Forms". In: *Pharm Res* 15.1 (Jan. 1998), pp. 11–22. ISSN: 0724-8741, 1573-904X. DOI: 10.1023/A:1011984216775. URL: http://link.springer.com/article/10.1023/A:1011984216775.

[26] S. Dvinskikh et al. "Anisotropic self-diffusion in thermotropic liquid crystals studied by ^{1}H and ^{2}H pulse-field-gradient spin-echo NMR". In: *Physical Review E* 65.6 (June 2002). ISSN: 1063-651X, 1095-3787. DOI: 10.1103/PhysRevE.65.061701. URL: http://link.aps.org/doi/10.1103/PhysRevE.65.061701.

[27] Marion Erpelding, Axelle Amon, and Jérôme Crassous. "Diffusive wave spectroscopy applied to the spatially resolved deformation of a solid". In: *Physical Review E* 78.4 (Oct. 2008). ISSN: 1539-3755, 1550-2376. DOI: 10.1103/PhysRevE.78.046104. URL: http://link.aps.org/doi/10.1103/PhysRevE.78.046104.

[28] Alfred Fahr and Xiangli Liu. "Drug delivery strategies for poorly water-soluble drugs". In: *Expert Opinion on Drug Delivery* 4.4 (July 2007), pp. 403–416. ISSN: 1742-5247, 1744-7593. DOI: 10.1517/17425247.4.4.403. URL: http://informahealthcare.com/doi/abs/10.1517/17425247.4.4.403.

[29] Gerald G. Fuller and Jan Vermant. "Complex Fluid-Fluid Interfaces: Rheology and Structure". In: *Annual Review of Chemical and Biomolecular Engineering* 3.1 (2012), pp. 519–543. DOI: 10.1146/annurev-chembioeng-061010-114202. URL: http://dx.doi.org/10.1146/annurev-chembioeng-061010-114202.

[30] Hu Gang et al. "Emulsion glasses: A dynamic light-scattering study". In: *Physical Review E* 59.1 (1999), p. 715. URL: http://pre.aps.org/abstract/PRE/v59/i1/p715_1.

[31] Lei Gao, Dianrui Zhang, and Minghui Chen. "Drug nanocrystals for the formulation of poorly soluble drugs and its application as a potential drug delivery system". In: *J Nanopart Res* 10.5 (May 2008), pp. 845–862. ISSN: 1388-0764, 1572-896X. DOI: 10.1007/s11051-008-9357-4. URL: http://link.springer.com/article/10.1007/s11051-008-9357-4.

[32] Satish K. Goel and Eric J. Beckman. "Generation of microcellular polymeric foams using supercritical carbon dioxide. I: Effect of pressure and temperature on nucleation". In: *Polymer Engineering & Science* 34.14 (1994), pp. 1137–1147. ISSN: 1548-2634. DOI: 10.1002/pen.760341407. URL: http://onlinelibrary.wiley.com/doi/10.1002/pen.760341407/abstract.

[33] William M Haynes and Chemical Rubber Company. "Compressibility and Expansion Coefficients of Liquids". English. In: *CRC handbook of chemistry and physics: a ready-reference book of chemical and physical data*. Boca Raton, Fla.; London: CRC Press, 2013. ISBN: 9781466571143 1466571144.

[34] M. Holz and H. Weingartner. "Calibration in accurate spin-echo self-diffusion measurements using ^{1}H and less-common nuclei". In: *Journal of Magnetic Resonance (1969)* 92.1 (1991), pp. 115–125. URL: http://www.sciencedirect.com/science/article/pii/002223649190252O.

[35] Manfred Holz, Stefan R. Heil, and Antonio Sacco. "Temperature-dependent self-diffusion coefficients of water and six selected molecular liquids for calibration in accurate 1H NMR PFG measurements". In: *Physical Chemistry Chemical Physics* 2.20 (2000), pp. 4740–4742. ISSN: 14639076, 14639084. DOI: 10.1039/b005319h. URL: http://xlink.rsc.org/?DOI=b005319h.

[36] Dieter Horn and Jens Rieger. "Organic Nanoparticles in the Aqueous Phase–Theory, Experiment, and Use". In: *Angewandte Chemie International Edition* 40.23 (2001), pp. 4330–4361. ISSN: 1521-3773. DOI: 10.1002/1521-3773(20011203)40:23<4330::AID-ANIE4330>3.0.CO;2-W. URL: http://onlinelibrary.wiley.com/doi/10.1002/1521-3773(20011203)40:23%3C4330::AID-ANIE4330%3E3.0.CO;2-W/abstract.

[37] C. Huh and S. G. Mason. "A rigorous theory of ring tensiometry". In: *Colloid & Polymer Sci* 253.7 (July 1975), pp. 566–580. ISSN: 0303-402X, 1435-1536. DOI: 10.1007/BF01753960. URL: http://link.springer.com/article/10.1007/BF01753960.

[38] C. Huh and S. G. Mason. "A rigorous theory of ring tensiometry: Addendum on the wall effect". In: *Colloid & Polymer Sci* 255.5 (May 1977), pp. 460–467. ISSN: 0303-402X, 1435-1536. DOI: 10.1007/BF01536462. URL: http://link.springer.com/article/10.1007/BF01536462.

[39] M. D. Hürlimann. "Optimization of timing in the Carr-Purcell-Meiboom-Gill sequence". In: *Magnetic resonance imaging* 19.3 (2001), pp. 375–378. DOI: 10.1016/S0730-725X(01)00251-X. URL: http://www.sciencedirect.com/science/article/pii/S0730725X0100251X.

[40] M.D. Hürlimann. "Carr–Purcell Sequences with Composite Pulses". In: *Journal of Magnetic Resonance* 152.1 (Sept. 2001), pp. 109–123. ISSN: 10907807. DOI: 10.1006/jmre.2001.2370. URL: http://linkinghub.elsevier.com/retrieve/pii/S1090780701923705.

[41] Leon J. M. Jacobs, Maartje F. Kemmere, and Jos T. F. Keurentjes. "Sustainable polymer foaming using high pressure carbon dioxide: a review on fundamentals, processes and applications". In: *Green Chem.* 10.7 (July 2008), pp. 731–738. ISSN: 1463-9270. DOI: 10.1039/B801895B. URL: http://pubs.rsc.org/en/content/articlelanding/2008/gc/b801895b.

[42] Sheng Jiang et al. "Seeding as a means of controlling particle size in dispersion polymerization". In: *Journal of Applied Polymer Science* 108.6 (June 2008), pp. 4096–4107. ISSN: 00218995, 10974628. DOI: 10.1002/app.28027. URL: http://doi.wiley.com/10.1002/app.28027.

[43] Gyan P. Johari. "Intrinsic mobility of molecular glasses". In: *The Journal of Chemical Physics* 58.4 (Aug. 1973), pp. 1766–1770. ISSN: 0021-9606, 1089-7690. DOI: 10.1063/1.1679421. URL: http://scitation.aip.org.ezp-prod1.hul.harvard.edu/content/aip/journal/jcp/58/4/10.1063/1.1679421 (visited on 02/21/2014).

[44] Gyan P. Johari and Martin Goldstein. "Viscous Liquids and the Glass Transition. II. Secondary Relaxations in Glasses of Rigid Molecules". In: *The Journal of Chemical Physics* 53.6 (Sept. 1970), pp. 2372–2388. ISSN: 0021-9606, 1089-7690. DOI: 10.1063/1.1674335. URL: http://scitation.aip.org/content/aip/journal/jcp/53/6/10.1063/1.1674335.

[45] Evangelos Karavas et al. "Investigation of the release mechanism of a sparingly water-soluble drug from solid dispersions in hydrophilic carriers based on physical state of drug, particle size distribution and drug–polymer interactions". In: *European Journal of Pharmaceutics and Biopharmaceutics* 66.3 (June 2007), pp. 334–347. ISSN: 09396411. DOI: 10.1016/j.ejpb.2006.11.020. URL: http://linkinghub.elsevier.com/retrieve/pii/S0939641106003390.

[46] V.V. Krishnan and Nagarajan Murali. "Radiation damping in modern NMR experiments: Progress and challenges". In: *Progress in Nuclear Magnetic Resonance Spectroscopy* 68 (Jan. 2013), pp. 41–57. ISSN: 00796565. DOI: 10.1016/j.pnmrs.2012.06.001. URL: http://linkinghub.elsevier.com/retrieve/pii/S0079656512000696.

[47] Martin-D. Lacasse, Gary S. Grest, and Dov Levine. "Deformation of small compressed droplets". In: *Physical Review E* 54.5 (1996), p. 5436. URL: http://pre.aps.org/abstract/PRE/v54/i5/p5436_1.

[48] Martin-D. Lacasse et al. "Model for the elasticity of compressed emulsions". In: *Physical review letters* 76.18 (1996), p. 3448. URL: http://prl.aps.org/abstract/PRL/v76/i18/p3448_1.

[49] Zoe A. Langham et al. "Mechanistic insights into the dissolution of spray-dried amorphous solid dispersions". In: *Journal of Pharmaceutical Sciences* 101.8 (Aug. 2012), pp. 2798–2810. ISSN: 00223549. DOI: 10.1002/jps.23192. URL: http://doi.wiley.com/10.1002/jps.23192.

[50] F. Leal-Calderon and V. Schmitt. "Solid-stabilized emulsions". In: *Current Opinion in Colloid & Interface Science* 13.4 (Aug. 2008), pp. 217–227. ISSN: 1359-0294. DOI: 10.1016/j.cocis.2007.09.005. URL: http://www.sciencedirect.com/science/article/pii/S1359029407001331.

[51] Ki-Chang Lee and Han-Ah Wi. "Influence of *n*-dodecyl mercaptan as chain transfer agent in dispersion polymerization of styrene". In: *Journal of Polymer Science Part A: Polymer Chemistry* 46.19 (Oct. 2008), pp. 6612–6620. ISSN:

0887624X, 10990518. DOI: 10.1002/pola.22971. URL: http://doi.wiley.com/10.1002/pola.22971.

[52] Ralf Lenke, Ralf Tweer, and Georg Maret. "Coherent backscattering of turbid samples containing large Mie spheres". In: *J. Opt. A: Pure Appl. Opt.* 4.3 (May 2002), p. 293. ISSN: 1464-4258. DOI: 10.1088/1464-4258/4/3/313. URL: http://iopscience.iop.org/1464-4258/4/3/313.

[53] Christian Leuner and Jennifer Dressman. "Improving drug solubility for oral delivery using solid dispersions". In: *European Journal of Pharmaceutics and Biopharmaceutics* 50.1 (July 2000), pp. 47–60. ISSN: 0939-6411. DOI: 10.1016/S0939-6411(00)00076-X. URL: http://www.sciencedirect.com/science/article/pii/S093964110000076X.

[54] Malcolm H. Levitt. "Composite pulses". In: *Progress in Nuclear Magnetic Resonance Spectroscopy* 18.2 (1986), pp. 61–122. ISSN: 0079-6565. DOI: 10.1016/0079-6565(86)80005-X. URL: http://www.sciencedirect.com/science/article/pii/007965658680005X.

[55] Malcolm H. Levitt and Ray Freeman. "Compensation for pulse imperfections in NMR spin-echo experiments". In: *Journal of Magnetic Resonance (1969)* 43.1 (1981), pp. 65–80. URL: http://www.sciencedirect.com/science/article/pii/0022236481900822.

[56] David C. Lin, Noshir A. Langrana, and Bernard Yurke. "Force-displacement relationships for spherical inclusions in finite elastic media". In: *Journal of Applied Physics* 97.4 (2005), p. 043510. ISSN: 00218979. DOI: 10.1063/1.1847698. URL: http://link.aip.org/link/JAPIAU/v97/i4/p043510/s1&Agg=doi.

[57] Michael Linn et al. "Soluplus as an effective absorption enhancer of poorly soluble drugs in vitro and in vivo". In: *European Journal of Pharmaceutical Sciences* 45.3 (Feb. 2012), pp. 336–343. ISSN: 0928-0987. DOI: 10.1016/j.ejps.2011.11.025. URL: http://www.sciencedirect.com/science/article/pii/S0928098711004325.

[58] F. C. MacKintosh and Sajeev John. "Diffusing-wave spectroscopy and multiple scattering of light in correlated random media". In: *Phys. Rev. B* 40.4 (Aug. 1989), pp. 2383–2406. DOI: 10.1103/PhysRevB.40.2383. URL: http://link.aps.org/doi/10.1103/PhysRevB.40.2383.

[59] F. C. MacKintosh et al. "Polarization memory of multiply scattered light". In: *Phys. Rev. B* 40.13 (Nov. 1989), pp. 9342–9345. DOI: 10.1103/PhysRevB.40.9342. URL: http://link.aps.org/doi/10.1103/PhysRevB.40.9342.

[60] T. G. Mason, J. Bibette, and D. A. Weitz. "Elasticity of Compressed Emulsions". In: *Phys. Rev. Lett.* 75.10 (Sept. 1995), pp. 2051–2054. DOI: 10.1103/PhysRevLett.75.2051. URL: http://link.aps.org/doi/10.1103/PhysRevLett.75.2051.

[61] T. G. Mason, Hu Gang, and D. A. Weitz. "Diffusing-wave-spectroscopy measurements of viscoelasticity of complex fluids". In: *J. Opt. Soc. Am. A* 14.1 (Jan. 1997), pp. 139–149. DOI: 10.1364/JOSAA.14.000139. URL: http://josaa.osa.org/abstract.cfm?URI=josaa-14-1-139.

[62] T. G. Mason et al. "Osmotic pressure and viscoelastic shear moduli of concentrated emulsions". In: *Physical Review E* 56.3 (1997), p. 3150. URL: http://pre.aps.org/abstract/PRE/v56/i3/p3150_1.

[63] J. Mattsson et al. "Influence of Chain Length on the α–β Bifurcation in Oligomeric Glass Formers". In: *Phys. Rev. Lett.* 94.16 (Apr. 2005), p. 165701. DOI: 10.1103/PhysRevLett.94.165701. URL: http://link.aps.org/doi/10.1103/PhysRevLett.94.165701.

[64] Elaine M. Merisko-Liversidge and Gary G. Liversidge. "Drug Nanoparticles: Formulating Poorly Water-Soluble Compounds". In: *Toxicol Pathol* 36.1 (Jan. 2008). PMID: 18337220, pp. 43–48. ISSN: 0192-6233, 1533-1601. DOI: 10.1177/0192623307310946. URL: http://tpx.sagepub.com/content/36/1/43.

[65] P. Mills and P. Snabre. "Settling of a suspension of hard spheres". In: *Europhysics Letters* 25.9 (1994), p. 651. URL: http://iopscience.iop.org/0295-5075/25/9/003.

[66] Javier O. Morales, Alan B Watts, and Jason T McConville. "Mechanical Particle-Size Reduction Techniques". In: *Formulating Poorly Water Soluble Drugs*. AAPS Advances in the Pharmaceutical Sciences Series 3. AAPS Press, 2012. ISBN: 978-1-4614-1144-4. URL: http://www.springer.com/biomed/pharmacology+&+toxicology/book/978-1-4614-1143-7.

[67] Anthony James Paine, Wayne Luymes, and James McNulty. "Dispersion polymerization of styrene in polar solvents. 6. Influence of reaction parameters on particle size and molecular weight in poly (N-vinylpyrrolidone)-stabilized reactions". In: *Macromolecules* 23.12 (1990), pp. 3104–3109. URL: http://pubs.acs.org/doi/abs/10.1021/ma00214a012.

[68] Chul B. Park, Daniel F. Baldwin, and Nam P. Suh. "Effect of the pressure drop rate on cell nucleation in continuous processing of microcellular polymers". In: *Polymer Engineering & Science* 35.5 (1995), pp. 432–440. ISSN: 1548-2634. DOI: 10.1002/pen.760350509. URL: http://onlinelibrary.wiley.com/doi/10.1002/pen.760350509/abstract.

[69] Leena Peltonen and Jouni Hirvonen. "Pharmaceutical nanocrystals by nanomilling: critical process parameters, particle fracturing and stabilization methods". In: *Journal of Pharmacy and Pharmacology* 62.11 (2010), pp. 1569–1579. ISSN: 2042-7158. DOI: 10.1111/j.2042-7158.2010.01022.x. URL: http://onlinelibrary.wiley.com/doi/10.1111/j.2042-7158.2010.01022.x/abstract.

[70] Roberto Piazza, Tommaso Bellini, and Vittorio Degiorgio. "Equilibrium sedimentation profiles of screened charged colloids: A test of the hard-sphere equation of state". In: *Physical review letters* 71.25 (1993), p. 4267. URL: http://prl.aps.org/abstract/PRL/v71/i25/p4267_1.

[71] Spencer Umfreville Pickering. "CXCVI.–Emulsions". In: *Journal of the Chemical Society, Transactions* 91 (Jan. 1907), pp. 2001–2021. ISSN: 0368-1645. DOI: 10.1039/CT9079102001. URL: http://pubs.rsc.org/en/content/articlelanding/1907/ct/ct9079102001.

[72] William S. Price. "Pulsed-field gradient nuclear magnetic resonance as a tool for studying translational diffusion: Part 1. Basic theory". In: *Concepts in Magnetic Resonance* 9.5 (1997), pp. 299–336. ISSN: 1099-0534. DOI: 10.1002/(SICI)1099-0534(1997)9:5<299::AID-CMR2>3.0.CO;2-U. URL: http://onlinelibrary.wiley.com/doi/10.1002/(SICI)1099-0534(1997)9:5%3C299::AID-CMR2%3E3.0.CO;2-U/abstract.

[73] William S. Price. "Pulsed-field gradient nuclear magnetic resonance as a tool for studying translational diffusion: Part II. Experimental aspects". In: *Concepts in Magnetic Resonance* 10.4 (1998), pp. 197–237. ISSN: 1099-0534. DOI: 10.1002/(SICI)1099-0534(1998)10:4<197::AID-CMR1>3.0.CO;2-S. URL: http://onlinelibrary.wiley.com/doi/10.1002/(SICI)1099-0534(1998)10:4%3C197::AID-CMR1%3E3.0.CO;2-S/abstract.

[74] H. M. Princen and A. D. Kiss. "Osmotic pressure of foams and highly concentrated emulsions. 2. Determination from the variation in volume fraction with height in an equilibrated column". In: *Langmuir* 3.1 (Jan. 1987), pp. 36–41. ISSN: 0743-7463. DOI: 10.1021/la00073a007. URL: http://dx.doi.org/10.1021/la00073a007.

[75] H. M. Princen and A. D. Kiss. "Rheology of foams and highly concentrated emulsions: III. Static shear modulus". In: *Journal of colloid and interface science* 112.2 (1986), pp. 427–437. URL: http://www.sciencedirect.com/science/article/pii/0021979786901116.

[76] H. M Princen and A. D Kiss. "Rheology of foams and highly concentrated emulsions: IV. An experimental study of the shear viscosity and yield stress of concentrated emulsions". In: *Journal of Colloid and Interface Science* 128.1 (Mar. 1989), pp. 176–187. ISSN: 0021-9797. DOI: 10.1016/0021-9797(89)90396-2. URL: http://www.sciencedirect.com/science/article/pii/0021979789903962.

[77] W. Ramsden. "Separation of Solids in the Surface-Layers of Solutions and 'Suspensions' (Observations on Surface-Membranes, Bubbles, Emulsions, and Mechanical Coagulation). – Preliminary Account". In: *Proceedings of the Royal Society of London* 72.477-486 (Jan. 1903), pp. 156–164. ISSN: 0370-1662, DOI:

10.1098/rspl.1903.0034. URL: http://rspl.royalsocietypublishing.org/content/72/477-486/156.

[78] Luis Fernando Rojas-Ochoa et al. "Depolarization of backscattered linearly polarized light". In: *JOSA A* 21.9 (2004), pp. 1799–1804. URL: http://www.opticsinfobase.org/abstract.cfm?id=80935.

[79] M. C. W. van Rossum and Th. M. Nieuwenhuizen. "Multiple scattering of classical waves: microscopy, mesoscopy, and diffusion". In: *Rev. Mod. Phys.* 71.1 (Jan. 1999), pp. 313–371. DOI: 10.1103/RevModPhys.71.313. URL: http://link.aps.org/doi/10.1103/RevModPhys.71.313.

[80] Jasmine M. Rowe and Keith P. Johnson. "Precipitation Technologies for Nanoparticle Production". In: *Formulating Poorly Water Soluble Drugs*. AAPS Advances in the Pharmaceutical Sciences Series 3. AAPS Press, 2012. ISBN: 978-1-4614-1144-4. URL: http://www.springer.com/biomed/pharmacology+&+toxicology/book/978-1-4614-1143-7.

[81] M. A. Rutgers et al. "Measurement of the hard-sphere equation of state using screened charged polystyrene colloids". In: *Physical Review B* 53.9 (1996), p. 5043. URL: http://prb.aps.org/abstract/PRB/v53/i9/p5043_1.

[82] A. Saint-Jalmes and D. J. Durian. "Vanishing elasticity for wet foams: Equivalence with emulsions and role of polydispersity". In: *Journal of Rheology* 43.6 (1999), p. 1411. ISSN: 01486055. DOI: 10.1122/1.551052. URL: http://link.aip.org/link/JORHD2/v43/i6/p1411/s1&Agg=doi.

[83] Pabitra N. Sen. "Time-dependent diffusion coefficient as a probe of geometry". In: *Concepts in Magnetic Resonance* 23A.1 (Sept. 2004), pp. 1–21. ISSN: 1043-7347, 1099-0534. DOI: 10.1002/cmr.a.20017. URL: http://doi.wiley.com/10.1002/cmr.a.20017.

[84] Anand Bala Subramaniam et al. "Mechanics of interfacial composite materials". In: *Langmuir* 22.24 (2006), pp. 10204–10208. URL: http://pubs.acs.org/doi/abs/10.1021/la061475s.

[85] David L. Tomasko et al. "A Review of CO2 Applications in the Processing of Polymers". In: *Ind. Eng. Chem. Res.* 42.25 (Dec. 2003), pp. 6431–6456. ISSN: 0888-5885. DOI: 10.1021/ie030199z. URL: http://dx.doi.org/10.1021/ie030199z.

[86] H. C. Torrey. "Bloch Equations with Diffusion Terms". In: *Phys. Rev.* 104.3 (Nov. 1956), pp. 563–565. DOI: 10.1103/PhysRev.104.563. URL: http://link.aps.org/doi/10.1103/PhysRev.104.563.

[87] D Vella, P Aussillous, and L Mahadevan. "Elasticity of an interfacial particle raft". In: *Europhysics Letters (EPL)* 68.2 (Oct. 2004), pp. 212–218. ISSN: 0295-5075, 1286-4854. DOI: 10.1209/epl/i2004-10202-x. URL: http://stacks.iop.org/0295-5075/68/i=2/a=212?key=crossref.cc740c886ef8a8e5a3aa883fec29b9c3.

[88] Moin U. Vera, Arnaud Saint-Jalmes, and Douglas J. Durian. "Scattering optics of foam". In: *Applied optics* 40.24 (2001), pp. 4210–4214. URL: http://www.opticsinfobase.org/abstract.cfm?&id=65065.

[89] Geert Verreck et al. "The effect of pressurized carbon dioxide as a temporary plasticizer and foaming agent on the hot stage extrusion process and extrudate properties of solid dispersions of itraconazole with PVP-VA 64". In: *European Journal of Pharmaceutical Sciences* 26.3–4 (Nov. 2005), pp. 349–358. ISSN: 0928-0987. DOI: 10.1016/j.ejps.2005.07.006. URL: http://www.sciencedirect.com/science/article/pii/S0928098705002277.

[90] Virgile Viasnoff, François Lequeux, and D. J. Pine. "Multispeckle diffusing-wave spectroscopy: A tool to study slow relaxation and time-dependent dynamics". In: *Review of Scientific Instruments* 73.6 (2002), p. 2336. ISSN: 00346748. DOI: 10.1063/1.1476699. URL: http://link.aip.org/link/RSINAK/v73/i6/p2336/s1&Agg=doi.

[91] Goran T. Vladisavljević and Helmar Schubert. "Influence of process parameters on droplet size distribution in SPG membrane emulsification and stability of prepared emulsion droplets". In: *Journal of Membrane Science* 225.1–2 (Nov. 2003), pp. 15–23. ISSN: 0376-7388. DOI: 10.1016/S0376-7388(03)00212-6. URL: http://www.sciencedirect.com/science/article/pii/S0376738803002126.

[92] Jianling Wang and Laszlo Urban. "The impact of early ADME profiling on drug discovery and development strategy". In: *Drug Discovery World* 5.4 (2004), pp. 73–86. URL: http://www.ddw-online.com/media/32/2460/04.fal.the-impact-of-early-adme-profiling-on-drug-discovery-and-development-strategy.pdf.

[93] David A. Weitz and David J. Pine. "Diffusing-wave spectroscopy". In: *Dynamic light scattering: the method and some applications*. Oxford [England]; New York: Clarendon Press ; Oxford University Press, 1993, pp. 652–720. ISBN: 0198539428 9780198539421.

[94] M. Xu and R. Alfano. "Random Walk of Polarized Light in Turbid Media". In: *Physical Review Letters* 95.21 (Nov. 2005). ISSN: 0031-9007, 1079-7114. DOI: 10.1103/PhysRevLett.95.213901. URL: http://link.aps.org/doi/10.1103/PhysRevLett.95.213901.

[95] Lukasz J. Zielinski and Pabitra N. Sen. "Combined effects of diffusion, nonuniform-gradient magnetic fields, and restriction on an arbitrary coherence pathway". In: *The Journal of Chemical Physics* 119.2 (2003), p. 1093. ISSN: 00219606. DOI: 10.1063/1.1578615. URL: http://link.aip.org/link/JCPSA6/v119/i2/p1093/s1&Agg=doi.

[96] Lukasz J. Zielinski and Pabitra N. Sen. "Effects of finite-width pulses in the pulsed-field gradient measurement of the diffusion coefficient in connected porous media". In: *Journal of Magnetic Resonance* 165.1 (Nov. 2003), pp. 153–161. ISSN: 10907807. DOI: 10.1016/S1090-7807(03)00248-9. URL: http://linkinghub.elsevier.com/retrieve/pii/S1090780703002489.

[97] Lukasz J Zielinski and Pabitra N Sen. "Relaxation of Nuclear Magnetization in a Nonuniform Magnetic Field Gradient and in a Restricted Geometry". In: *Journal of Magnetic Resonance* 147.1 (Nov. 2000), pp. 95–103. ISSN: 10907807. DOI: 10.1006/jmre.2000.2185. URL: http://linkinghub.elsevier.com/retrieve/pii/S1090780700921852.